Author(s): Ollila, Santtu T. T. & Smith, Christopher J. & Ala-Nissilä, Tapio & Denniston, Colin

Title: The Hydrodynamic Radius of Particles in the Hybrid Lattice Boltzmann-Molecular Dynamics Method

Year: 2013

Version: Final published version

Please cite the original version:

Ollila, Santtu T. T. & Smith, Christopher J. & Ala-Nissilä, Tapio & Denniston, Colin. 2013. The Hydrodynamic Radius of Particles in the Hybrid Lattice Boltzmann-Molecular Dynamics Method. Multiscale Modeling & Simulation. Volume 11, Issue 1. P. 213-243. ISSN 1540-3459 (printed). DOI: 10.1137/110858756.

Multiscale Model. Simul.
Vol. 11, No. 1, pp. 213–243

THE HYDRODYNAMIC RADIUS OF PARTICLES IN THE HYBRID LATTICE BOLTZMANN–MOLECULAR DYNAMICS METHOD[*]

SANTTU T. T. OLLILA[†][‡], CHRISTOPHER J. SMITH[†], TAPIO ALA-NISSILA[‡][§], AND COLIN DENNISTON[†]

Abstract. We address the problem of the consistency of different measures of the hydrodynamic radius of solid point and composite solute particles incorporated into the hybrid lattice Boltzmann–molecular dynamics (LBMD) multiscale method. The coupling between the fluid and the particle phase is naturally implemented through a Stokesian type of frictional force proportional to the local velocity difference between the two. Using deterministic flow tests such as measuring the Stokes drag, hydrodynamic torques, and forces we first demonstrate that in this case the hydrodynamic size of the particles is ill-defined in the existing LBMD schemes. We then show how it is possible to effectively achieve the no-slip limit in a discrete simulation with a finite coefficient of the frictional force by demanding consistency of all these measures, but this requires a somewhat modified LB algorithm for numerical stability. Having fulfilled the criteria, we further show that in our consistent coupling scheme particles also obey the *macroscopically observed* fluctuation-dissipation theorem for the diffusion coefficient of a single particle without any adjustable parameters. In addition, we explicitly show that diffusion alone is not a good criterion for calibration of the frictional coupling.

Key words. hydrodynamics, complex fluids, hydrodynamic consistency, limit of impermeability

AMS subject classifications. 76T20, 76R50, 76M28

DOI. 10.1137/110858756

1. Introduction.

Hydrodynamic interactions between solute particles, from the microscopic to the macroscopic scale, are important from both the scientific and industrial standpoints [1]. Traditionally, colloidal suspensions appear in a wide range of products, from the food and drug industry to paint manufacturing and aerosols. Most recently, nanofluids, i.e., fluids with nanometer size solute particles, have been under intense study due to their extraordinary properties [2]. Many industrial processes rely on the firm understanding of the rheological properties of suspensions. Measuring interactions of individual particles within suspensions of large numbers of particles is currently unfeasible in an experimental framework except for a few specialized situations. This makes the use of theory and simulations a key tool for understanding processes occurring in experiments. However, dealing with the required solution to the moving fluid-solid boundary problem in theory and simulation is still an ongoing problem for which there is no well-established "standard" algorithmic solution. For flexible particles, or polymers in solution, there are also disparate time scales for the evolution of the intraparticle dynamics and the hydrodynamics that affect long-time behavior. This suggests the need for a multiscale technique that deals with these degrees of freedom with different, but coupled methods.

---

[*] Received by the editors December 13, 2011; accepted for publication (in revised form) October 31, 2012; published electronically January 29, 2013. This work was supported by the Academy of Finland through its COMP Centre of Excellence Program (project 251748), by the Natural Science and Engineering Council of Canada, and by SharcNet.
http://www.siam.org/journals/mms/11-1/85875.html

[†] Department of Applied Mathematics, The University of Western Ontario, London, ON N6A 5B7, Canada (santtu.ollila@aalto.fi, csmith8@uwo.ca, cdennist@uwo.ca). The first author's research was supported by Magnus Ehrnrooth and the Alfred Kordelin Foundation.

[‡] COMP CoE at the Department of Applied Physics, Aalto University School of Science and Technology, FIN-00076 Aalto, Espoo, Finland (tapio.ala-nissila@tkk.fi).

[§] Department of Physics, Brown University, Providence, RI 02912-1843.

Most theoretical work on colloidal hydrodynamics comprises analytical steady state solutions in the "Stokes flow" regime (linearized hydrodynamics). The best known example is the hydrodynamic drag force on a single solid sphere moving at velocity $\mathbf{v}$ relative to a quiescent background fluid derived by Stokes in 1851 [3], $\mathbf{F}_s = 6\pi\eta a\mathbf{v}$, where η is the fluid viscosity and a is the radius. The hydrodynamic forces acting between two spheres at low Reynolds number have also been calculated by a number of authors [4, 5, 6, 7]. Oseen worked out the interaction between irrotational particles in a fluid at a distance r from one another [8], a result that was improved upon by Rotne and Prager for close particle interactions [9]. These Oseen-style tensors are valid at intermediate distances: when the particles are far apart, their validity breaks down as they assume instantaneous propagation of hydrodynamic interactions. There are cases where the finite propagation speed of hydrodynamic interactions has an effect, and it would clearly be useful to solve the full hydrodynamics rather than the linearized Stokesian approximation to deal with these cases.

The lattice Boltzmann (LB) method has been used successfully in solving the general nonlinear problem involving a compressible fluid [10, 11, 12, 13, 14]. Linear interpolation has been used to incorporate a moving boundary into an LB simulation [15, 16] together with a drag force to make the fluid velocity at the solid "boundary" and the particle velocity track each other. This yields a multiscale simulation where the dynamics of the flexible surface are updated using a molecular dynamics (MD) simulation and the hydrodynamics evolve using LB, potentially with a much longer time step. Peskin and coworkers have also done extensive work on incorporating boundaries in incompressible fluids by effective interpolation onto the discretized mesh of the fluid and, in particular, on how to eliminate the resulting mesh effects [17, 18, 19, 20]. The key to their immersed boundary method is an efficient and well-chosen discrete representation of the Dirac delta function with compact support on the fluid mesh. Cates and collaborators have incorporated this scheme into an LB simulation for point particles [21].

For these hybrid lattice Boltzmann–molecular dynamics (LBMD) methods to work properly, they should give consistent results for hydrodynamic measurements for solvable cases of particles in flow. To test the physical consistency and accuracy of any of the methods for simulating impermeable solute particles one needs to consider the fundamental concept of a hydrodynamic radius a_h. It can be determined through measuring quantities such as the drag force, hydrodynamic interactions between two or more particles, and the hydrodynamic torque on a particle. In fact, any measurement sensitive to the particle size could be used as a means of determining its hydrodynamic radius. However, within measurement error, all these definitions should yield the same result in the sense that the difference $|a_h - a'_h| < \Delta x$ between any two values of the radius a_h and a'_h (as obtained using different methods) should be less than the fluid mesh discretization Δx. An implicit assumption in most works is that one measure of hydrodynamic radius is equivalent to any other. However, there is currently no theoretical basis for this assumption; in fact in this paper we demonstrate that the consistency between deterministic measures of a_h is far from guaranteed in methods based on a frictional velocity coupling. To remedy this problem we provide criteria for calibration of the frictional coupling, which guarantees consistency between different definitions of a_h. We also construct a finite-difference scheme that enables the use of large coupling parameters in a wider range of circumstances.

The definition of a_h is further complicated in the case when thermal fluctuations are coupled to the LB method [22, 23]. This is because the Brownian tracer diffusion coefficient of a single colloidal particle D is inversely proportional to a_h, and thus

D constitutes one possible measure of a_h. Ahlrichs and Dünweg [24, 25] found that thermally induced particle motion did not obey the fluctuation-dissipation theorem consistent with the temperature of the fluid and the drag force experienced by a single particle. They corrected this by adding a Langevin thermostat directly to the particle phase, which goes against Einstein's original physical idea of the origin of Brownian motion being *in the solvent* surrounding the suspended particles [26]. To maintain momentum conservation, they then added noise locally to the fluid but with a sign opposite to that of the noise on the particle [24, 25]. Concerning the case with thermal fluctuations, we argue here that *in the no-slip limit* the imposition of diverging external Langevin noise causes unphysical thermal fluctuations and correlations in the fluid that has an impact when particles are closely packed.

We show that by fixing the parameters of the model using the aforementioned deterministic tests, *quantitative* agreement with the *macroscopic* fluctuation-dissipation relation, including finite-size corrections, for the diffusion of a single particle follows if the thermal fluctuations are implemented as presented in [23]. This means that no Langevin noise needs to be added in the solutes, which is an important conceptual development for the LB methodology. Moreover, this result extends the applicability of particles in the LB method to dense, strongly correlated systems [23].

Section 2 of this paper explains the fluid model that we use, followed by section 3, which describes how solid inclusions are coupled to the fluid mesh. The theory pertaining to different measures of hydrodynamic radius is presented in section 4, which provides the necessary background for the results of section 5. We conclude the paper in section 6 and discuss the implications of our work.

2. Fluid model.

The mass and momentum conservation in a fluid are expressed at the Navier–Stokes level as [5, 27]

$$\partial_t \rho + \partial_\alpha(\rho u_\alpha) = 0 \tag{2.1}$$

and

$$\begin{aligned} \partial_t(\rho u_\alpha) + \partial_\beta(\rho u_\alpha u_\beta) &= -\partial_\alpha P_{\alpha\beta} + F_\alpha \\ &+ \partial_\beta \left(\eta \left(\partial_\alpha u_\beta + \partial_\beta u_\alpha - \frac{2}{3}\partial_\gamma u_\gamma \delta_{\alpha\beta} \right) + \zeta \partial_\gamma u_\gamma \delta_{\alpha\beta} \right), \end{aligned} \tag{2.2}$$

where ρ and u_α are the fluid density and components of velocity, η and ζ are the shear and bulk viscosities, and $P_{\alpha\beta}$ is the fluid pressure. In this work we will use a diagonal pressure tensor with linear dependence on density, i.e., $P_{\alpha\beta} = \rho v_s^2 \delta_{\alpha\beta}$, where v_s is the speed of sound. This can be viewed as an ideal gas equation of state or the first term in a Taylor expansion of the pressure about fixed density in which case v_s^2 is the isentropic compressibility [28]. External force densities, such as gravity, appear through F_α. Our LB fluid algorithm reproduces (2.1) and (2.2) in the form typical to most LB algorithms [29]. The shear viscosity in the model is $\eta = \rho\tau v_c^2/3$, where $v_c = \Delta x/\Delta t$ is a lattice velocity, and $\zeta = \eta(5/3 - 3v_s^2/v_c^2)$ [11]. In this paper, τ will be chosen in all cases so that $\eta = 0.01\,\mathrm{g\,cm^{-1}s^{-1}}$, the viscosity of water, and $\rho = 1\,\mathrm{g\,cm^{-3}}$ (i.e., we set $\tau/\Delta t = 3\eta\Delta t/(\rho\Delta x^2)$). The speed of sound v_s is chosen sufficiently large so that the fluid is approximately incompressible (largest variation in $\rho < 0.1\%$ for $v_s = 1\,\mathrm{m\,s^{-1}}$), and in most cases we choose $v_s^2 = v_c^2/3$ ($v_s < v_c$ is required for stability in LB algorithms). Within the simulations themselves, computation is done in units of the lattice discretization Δx and Δt. In addition to body forces, $F_\alpha = F_\alpha(\mathbf{x}, t)$ includes local forces arising from the particle phase. Its implementation will be given in detail in the next section.

The LB method is an efficient way to solve the Navier–Stokes equations numerically [30, 31]. The method is based on solving an approximation of the Boltzmann transport equation (BE) on a structured lattice with sites $\mathbf{x} = (i, j, k)\Delta x$ connected to their neighboring sites by a set of vectors $\{\mathbf{e}_i\}_{i=0}^{n-1}$ along which material is transported according to a discretized version of the BE. We summarize a finite-difference LB scheme which results in (2.1) and (2.2) to fourth order in Δt and Δx, the time step, and spatial mesh resolution. The reader interested only in the results can safely skip over the remainder of this section. We define a distribution function $f_i(\mathbf{x}, t)$, where i labels the lattice directions from site $\mathbf{x}$. For three-dimensional systems, a 15-velocity model [30] on a cubic lattice with lattice vectors $\mathbf{e}_i = (0, 0, 0)$, $(\pm1, 0, 0)$, $(0, \pm1, 0)$, $(0, 0, \pm1)$, $(\pm1, \pm1, \pm1)v_c$ is chosen, where $v_c = \Delta x/\Delta t$. Physical variables are defined as moments of the distribution functions by

$$\rho(\mathbf{x}, t) \equiv \sum_i f_i(\mathbf{x}, t), \quad (\rho u_\alpha)(\mathbf{x}, t) \equiv \sum_i f_i(\mathbf{x}, t) e_{i\alpha}. \tag{2.3}$$

The distribution functions evolve in time according to [32]

$$D_i f_i \equiv (\partial_t + e_{i\alpha}\partial_\alpha) f_i = -\frac{1}{\tau}\left(f_i - f_i^{eq}\right) + W_i, \tag{2.4}$$

where we have also defined the material derivative D_i and a driving term W_i. The exact solution of this PDE at time $t + \Delta t$ can be formally written as (see, e.g., [33, p. 3])

$$\begin{aligned} f_i(\mathbf{x} + \mathbf{e}_i\Delta t, t + \Delta t) &= e^{-\Delta t/\tau} f_i(\mathbf{x}, t) \\ &\quad + e^{-\Delta t/\tau} \int_t^{t+\Delta t} \frac{1}{\tau} e^{(s-t)/\tau} g_i^{\mathrm{eq}}(\mathbf{x} + \mathbf{e}_i s, t + s)\,\mathrm{d}s, \end{aligned} \tag{2.5}$$

where $g_i^{\mathrm{eq}} = f_i^{\mathrm{eq}} + \tau W_i$. Expanding $g^{\mathrm{eq}}(\mathbf{x} + \mathbf{e}_i s, t + s)$ as a Taylor series about $s = 0$ and integrating each term gives the following finite-difference scheme:

$$\begin{aligned} f_i(\mathbf{x} + \mathbf{e}_i\Delta t, t + \Delta t) &= g_i^{\mathrm{eq}}(\mathbf{x}, t) \\ &+ e^{-\Delta t/\tau}\left(f_i(\mathbf{x}, t) - g_i^{\mathrm{eq}}(\mathbf{x}, t)\right) \\ &+ \Delta t \left(1 - \frac{\tau}{\Delta t}\left(1 - e^{-\Delta t/\tau}\right)\right) D_i g_i^{\mathrm{eq}}(\mathbf{x}, t) \\ &+ \Delta t^2 \left(\frac{\tau^2}{\Delta t^2}\left(1 - e^{-\Delta t/\tau}\right) - \frac{\tau}{\Delta t} + \frac{1}{2}\right) D_i^2 g_i^{\mathrm{eq}}(\mathbf{x}, t) \\ &+ \mathcal{O}(\Delta t^4). \end{aligned} \tag{2.6}$$

We use this algorithm rather than the more standard Euler LB algorithm [34, 35, 30], as the solute forces (the forces the particles exert on the fluid) will effectively introduce stiff terms into the equation. Our algorithm eliminates the most troublesome Euler instabilities found in the standard LB scheme that result from adding solute forces, without adding significant complications. The coefficients are constants and are precomputed at the beginning of the code. The derivative $D_i g^{\mathrm{eq}}$ is evaluated as a backward finite difference,

$$D_i g_i^{\mathrm{eq}}(\mathbf{x}, t) \approx \frac{g_i^{\mathrm{eq}}(\mathbf{x}, t) - g_i^{\mathrm{eq}}(\mathbf{x} - \mathbf{e}_i\Delta t, t - \Delta t)}{\Delta t}, \tag{2.7}$$

and $D_i^2 g^{\mathrm{eq}}$ as

$$D_i^2 g^{\mathrm{eq}}(\mathbf{x},t) \approx \frac{D_i g_i^{\mathrm{eq}}(\mathbf{x}+\mathbf{e}_i\Delta t,t) - D_i g_i^{\mathrm{eq}}(\mathbf{x},t)}{\Delta t}. \tag{2.8}$$

The $\mathcal{O}(\Delta t)$ discretization error in $D_i g^{\mathrm{eq}}$ is $(\Delta t/2)D_i^2 g_i^{\mathrm{eq}}$, and this is taken into account by adding an appropriate term to the coefficient of the $D_i^2 g^{\mathrm{eq}}$ term. At the boundaries, computation is eased by noting that the D_i^2 term is zero at the boundary (assuming bounce-back is used). Also, at the boundary, (2.7) is evaluated as

$$D_i g_i^{\mathrm{eq}}(\mathbf{x},t) = (g_{-i}^{\mathrm{eq}}(\mathbf{x}-\mathbf{e}_i\Delta t,t) - g_i^{\mathrm{eq}}(\mathbf{x}-\mathbf{e}_i\Delta t,t-\Delta t))/\Delta t, \tag{2.9}$$

where $\mathbf{x}$ is the boundary node and $\mathbf{x}-\mathbf{e}_i\Delta t$ is in the bulk. The subscript $-i$ refers to the lattice direction opposite to i.

By choosing appropriate moments for the equilibrium distribution f_i^{eq} and the driving term W_i as

$$\begin{aligned} &\sum_i f_i^{\mathrm{eq}} = \rho; \qquad \sum_i f_i^{\mathrm{eq}} e_{i\alpha} = \rho u_\alpha;\\ &\sum_i f_i^{\mathrm{eq}} e_{i\alpha} e_{j\beta} = P_{\alpha\beta} + \rho u_\alpha u_\beta;\\ &\sum_i W_i = 0; \qquad \sum_i W_i e_{i\alpha} = F_\alpha;\\ &\sum_i W_i e_{i\alpha} e_{j\beta} = u_\alpha F_\beta + F_\alpha u_\beta, \end{aligned} \tag{2.10}$$

(2.1) and (2.2) can be obtained from (2.4) via a Chapman–Enskog expansion similar to derivations in [29]. We have included a simple derivation of the moments of the forcing terms in the appendix. Last, we want to emphasize that the results of present work are by no means specific to this finite-difference algorithm, but it allows a stronger coupling between the fluid and the MD particle. There can also be stability issues in the MD algorithm to move the particles, but for systems with only a few particles, such as those described in this paper, it is easy to implement a standard A-stable ODE solver [36]. A more general MD algorithm could also be constructed for a many-particle system along lines very similar to that of the LB algorithm described above which reverts to velocity-Verlet for conservative forces.

3. Node distribution algorithm.

Any surface included will have to be mapped onto the computational fluid mesh. A surface is first discretized to consist of a set of nodes, which is illustrated in Figure 3.1 in two dimensions for ease of visualization. We will refer to the points of the surface discretization as "surface nodes" and to the points of the fluid mesh as "mesh sites" or "lattice sites." The surface nodes are distributed to the corners of the fluid mesh plaquette in which they reside. This algorithm is similar to that used by Ahlrichs and Dünweg [24, 25] and that which we used successfully for objects in a liquid crystal [37]. To distribute the surface nodes, the ratio $\xi_{ij}^{(T)}$ of the opposing area to the total area of the cell is calculated and given to the corresponding mesh site (for instance, for surface node i and mesh site $j = P1$ in Figure 3.1, $\xi_{ij}^{(T)}$ is $A1/\Delta x^2$). This method is easily generalized to three dimensions, where the proportion of volumes will be used rather than areas. We refer to this method as the trilinear (T) node distribution algorithm or the trilinear stencil. By calculating the values of the weights in this manner, it is easily seen that the values

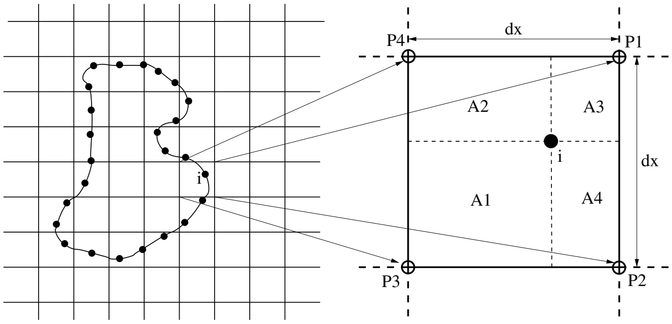

Fig. 3.1. *An example of a single node placed within a two-dimensional fluid mesh trilinearly. The solid circle is the location of the node, and the hollow circles are the fluid mesh sites. Each mesh site is affected by the surface node by the proportion of the opposite enclosed area relative to the area of the entire cell. (For example, $P1$ is affected from the surface node i by an amount $A1/\Delta x^2$.)*

of the node weights shift smoothly from zero, when the node is cross corner from the current fluid mesh site, to one, when the node passes through the mesh site in question. This is repeated for all surface nodes. As the surface of the solid travels through the lattice, its nodes affect the fluid mesh in a continuous manner. There are no discontinuities or jumps which need to be accounted for. Also, it is easy to simulate any arbitrary shape—there is nothing special about spheres. No further information is required about the surface as it moves through the system except for its linear and angular velocities. Knowing the surface normal where the surface intersects lattice links is not required.

Another widely used method for spreading nodes over mesh sites is the immersed boundary method [17, 18], which has been suggested for point solutes in [21]. Rather than using a distribution proportional to the node weights across the adjacent fluid mesh sites on the lattice, the immersed boundary method employs a smoothing kernel to spread the influence of the nodes represented by a force density onto a compact support and may be defined off-lattice. We use $\mathbf{r}$ for node locations as opposed to $\mathbf{x}$ to denote positions of lattice sites. Such a force density $\mathbf{s}(\mathbf{R}(\lambda))$ yields the total force $\mathbf{F}(\mathbf{r})$ on the object in the form

$$\mathbf{F}(\mathbf{r}) = \int \mathbf{s}(\mathbf{R}(\lambda))\hat{\delta}(\mathbf{r} - \mathbf{R}(\lambda))\,\mathrm{d}\lambda, \tag{3.1}$$

where the force is localized to some manifold described parametrically as $\mathbf{R} = \mathbf{R}(\lambda)$ and $\mathrm{d}\lambda$ is the measure on the manifold. The kernel function $\hat{\delta}$ is a representation of the Dirac delta function regularized on the grid described as

$$\hat{\delta}(\mathbf{r}) = \frac{1}{\Delta x^3}\phi\left(\frac{x}{\Delta x}\right)\phi\left(\frac{y}{\Delta x}\right)\phi\left(\frac{z}{\Delta x}\right). \tag{3.2}$$

The exact form of the kernel $\hat{\delta}$ is described by

$$\phi(\zeta) = \begin{cases} \phi_1(\zeta), & |\zeta| \le 1, \\ \phi_2(\zeta), & 1 \le |\zeta| \le 2, \\ 0 & \text{otherwise}, \end{cases} \tag{3.3}$$

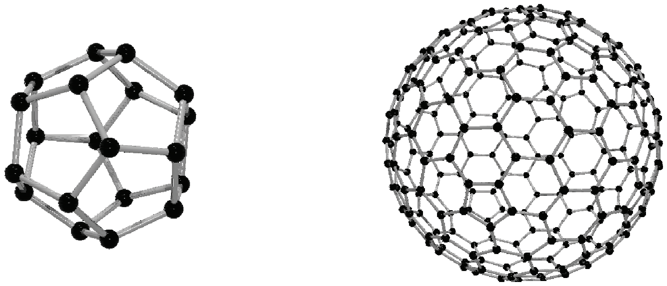

FIG. 3.2. *Example of two fullerenes. The left fullerene comprises* 20 *nodes, and the fullerene on the right has* 240 *nodes. Links between nodes are merely drawn in for visual aid. The node locations determine the surface with respect to the fluid mesh.*

where

$$\phi_1(\zeta) = \frac{1}{8}(3 - 2|\zeta| + \sqrt{1 + 4|\zeta| - 4|\zeta|^2}), \tag{3.4}$$

$$\phi_2(\zeta) = \frac{1}{8}(5 - 2|\zeta| + \sqrt{-7 + 12|\zeta| - 4|\zeta|^2}), \tag{3.5}$$

and ζ is the distance (in units of Δx) from the surface node i to the lattice site j in a given direction. From the description, each surface node affects the four nearest neighbors in the respective lattice mesh directions, amounting to a total of $n = 4^d$ affected mesh sites in d dimensions. This then implies

$$\xi_{ij}^{(P)} = \phi\left(\frac{x_{ij}}{\Delta x}\right) \phi\left(\frac{y_{ij}}{\Delta x}\right) \phi\left(\frac{z_{ij}}{\Delta x}\right), \tag{3.6}$$

the (x_{ij}, y_{ij}, z_{ij}) being the displacement vector from the fluid mesh site j to the surface node i. A derivation and a closed-form approximation to (3.3) can be found in [19]. Using both methods (trilinear (T) and Peskin (P)), we will compare and contrast to determine which is better under varying circumstances. We will also show what suffices for removal of lattice corrugation effects. Since the influence of each node is spread across a greater number of fluid mesh sites, one may assume the immersed boundary method is more accurate. An obvious disadvantage is that each node is spread across a greater number of fluid lattice sites, and thus at each time step more computational resources are spent describing the surface.

To mimic a sphere, we used the molecular shapes of fullerenes. The symmetry and regularity in their atomic structure make them ideal to be used as rigid shells for our purposes in trying to represent a sphere. The position of these nodes could easily be dictated by an MD style algorithm to allow the object's shape to deform, but we will not do that here. This differs from the algorithm of [15, 16], where they used a two-dimensional tethered bead-spring network with individual nodes connected to their nearest neighbors on the surface via finitely extensible nonlinear elastic springs and simply wrapped around a sphere. The rigidity of our spheres does not affect the forces involved with the hydrodynamics of the colloids at these sizes. Having access to a number of fullerenes of different sizes is convenient depending on the size of the sphere one wishes to place within the lattice [38]. A fullerene of $N_v = 20$ and one of 240 atoms are shown in Figure 3.2. In this paper, N_v denotes the number of nodes used to describe the inclusion. If the sphere is to traverse a large number of lattice cells, using a more resolved fullerene (bigger N_v) enables a denser placement of surface nodes. Having large gaps between surface nodes is to be avoided since the movement of fluid depends on the interaction between the lattice sites and surface nodes. That is, the discretization of the colloid surface should be finer than that of the fluid mesh.

As the surface moves through the fluid or the fluid itself is moving, an interaction must occur between the two media. The following is a synopsis of how interactions between the fluid mesh and the surface nodes are implemented. For the trilinear stencil, the approach is similar to that used in [39, 40]. The location of the surface nodes, $\mathbf{r}_i$, are calculated in relation to the center of mass of the solid. The velocity of each node is then calculated as $\mathbf{v}_i = \mathbf{v} + \mathbf{w} \times \mathbf{r}_i$, where $\mathbf{v}$ is the velocity of the center of mass of the solid, and $\mathbf{w}$ is the angular velocity of the solid. Using the method described in Figure 3.1, the ith surface node's weight ξ_{ij} is determined for the jth fluid mesh site which it affects. The set $\{\xi_{ij}\}$ is referred to as a stencil. A key property of any stencil for each surface node i is

$$\sum_{j=1}^{n} \xi_{ij} = 1, \tag{3.7}$$

where $n = 2^d$ in d dimensions for the trilinear method depicted in Figure 3.1, and $n = 4^d$ for the Peskin stencil (immersed boundary method). This ensures that if we were to use these weights to find the area of our sphere, we could do so exactly, independent of the fluid mesh resolution. This property reduces the lattice corrugations seen in most other methods [17].

The fluid velocities are known at each fluid mesh site. There are a couple of methods for computing the frictional force due to the fluid mesh sites on a surface node. The local forces at each fluid mesh site j affect the surface node i by

$$\mathbf{F}_{ij} = (\mathbf{v}_i - \hat{\mathbf{u}}_i)\xi_{ij}\gamma. \tag{3.8}$$

There is an apparent ambiguity in what velocity to use for $\hat{\mathbf{u}}_i$. The simplest choice is to use $\hat{\mathbf{u}}_i = \mathbf{u}(\mathbf{x}_j)$, the fluid velocity at the jth fluid mesh site (j is the index over the stencil). We call this the "noninterpolated" velocity. The other option is to use an "interpolated" fluid velocity at the position of the ith surface node,

$$\hat{\mathbf{u}}_i^{(I)} = \sum_{j=1}^{n} \xi_{ij}\mathbf{u}(\mathbf{x}_j), \tag{3.9}$$

where we abide to consistent use of either trilinear or Peskin interpolation of both the fluid velocity $\hat{\mathbf{u}}_i$ at the surface node location and the stencil $\{\xi_{ij}\}$. The interpolated velocity involves slightly more work, as two scans over the stencil are required, one to determine $\hat{\mathbf{u}}_i^{(I)}$ and one to compute (3.8). Using either of these velocities gives the same force on the ith surface node as

$$\mathbf{F}_i = \sum_{j=1}^{n} \mathbf{F}_{ij} = (\mathbf{v}_i - \hat{\mathbf{u}}_i^{(I)})\gamma, \tag{3.10}$$

making use of (3.7) for the "interpolated" case. However, this force is distributed differently onto the fluid mesh in the two cases and as a result leads to a slightly different fluid flow. As will be shown in section 5, the resulting steady state force ends up being slightly different as a result. The choice of $\hat{\mathbf{u}}$ affects the torque in particular, as will also be seen in section 5.

Note that $\mathbf{F}_i$ in (3.10) is not the Stokes drag force, as $\hat{\mathbf{u}}$ is not the far-field velocity. A direct consequence of this fact is that if the particle has radius a, even though one might guess choosing $\gamma = 6\pi\eta a$ would give the Stokes drag, this is not the case because of the discrepancy between the local velocity and the far-field velocity that go into the Stokes formula. Ahlrichs and Dünweg choose γ based on matching to Stokes drag (as inferred from a measurement of the diffusion coefficient) for a particle with a hydrodynamic radius decided a priori [24, 25]. We base our choice of γ on comparing several types of measurements of the hydrodynamic radius of a particle and demanding consistency between them. This leads to an effective no-slip boundary condition on the surface of our particle. The results of our investigations are described in section 5.

Performing a sum over the surface nodes,

$$\mathbf{F}_j = \sum_{i=1}^{N_v} \mathbf{F}_{ij}, \tag{3.11}$$

gives a three-dimensional mesh $\mathbf{F}_j = \mathbf{F}(\mathbf{x}_j)$ of local forces on the fluid which goes into (2.2) via (2.10). N_v is the number of surface nodes used to describe the solid. From here we can calculate the local forces $\mathbf{F}_i$ and torques $\mathbf{T}_i$ on each surface node by summing over the affected fluid mesh sites (i.e., over the stencil),

$$\mathbf{F}_i = \sum_{j=1}^{n} \mathbf{F}_{ij}, \qquad \mathbf{T}_i = \mathbf{r}_i \times \mathbf{F}_i, \tag{3.12}$$

or the net force and torque that the fluid exerts on the entire solid using

$$\mathbf{F} = \sum_{i=1}^{N_v} \mathbf{F}_i, \qquad \mathbf{T} = \sum_{i=1}^{N_v} \mathbf{T}_i, \tag{3.13}$$

where the N_v surface nodes belong to the same rigid body. Newton's third law is obeyed exactly.

To summarize, there are several algorithmic options that we plan to explore in the subsequent sections: first, there is the choice of stencil, trilinear or Peskin; second, there is the choice of $\hat{\mathbf{u}}_i$ in the force coupling, interpolated or noninterpolated; and finally, the value of γ must be determined. In section 5, we will compare the methods described in this section and evaluate their performance based on the theoretical predictions that we review next.

4. Theory.

In order to compare the different methods outlined in the previous section, and in particular in order to determine a physically consistent value for the key algorithmic parameter γ in the force coupling equation (3.8), we must compare to analytically known results that we summarize in this section. One key measure is to determine the "hydrodynamic" radius of both a single node (point particle) and a composite particle (like those in Figure 3.2). As we will see in the next section, different methods of measuring a hydrodynamic radius do not necessarily lead to mutually consistent values. We will consider three different means of determining the hydrodynamic radius of our particles: the drag force, viscous torques, and diffusion. In addition, we measure directly the hydrodynamic interactions between particles to ensure they are also quantitatively consistent with our other measures.

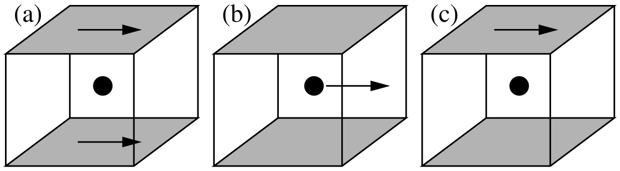

FIG. 4.1. *Schematic of geometries used to measure drag force and/or torque for a single particle in a box. There are walls on the top and bottom, and periodic boundaries in all other directions. In* (a) *the top and bottom walls are moving at speed v while the particle is held fixed. In* (b) *the walls are held stationary and the particle is moved at speed v through the center of the box. In* (c) *the bottom wall is stationary and the top wall is moved at speed v to generate a shear flow while the particle is held fixed.*

4.1. Analytic results for hydrodynamic interactions. Analytical expressions are available only for low Reynolds number flows, and finite-size effects must be considered by either constructing geometries that reduce them to a negligible level or by performing finite-size scaling. We outline the Stokes results and finite-size effects in this section. A single-particle Reynolds number can be defined by $Re = 2a\rho U/\eta$ in flows involving a spherical object of radius a and a characteristic fluid velocity U. Unless otherwise specified we will be using a single-particle Reynolds number (Re) less than 0.01. This is typically where inertial forces are very small, but viscous forces are relatively large. This allows us to compare our results to those derived from Stokes flow solutions of the forces on moving bodies. This constraint is imposed in order to compare to theory; it is not an intrinsic limitation of the LB scheme we are using. Once particles are free to move around and interact, a description in terms of a single Re is not possible. To ensure that we will always be in a regime appropriate for the anticipated applications of this method (colloidal and nanofluid dynamics), we will be using the viscosity and density of water for all simulations (i.e., water at S.T.P.).

For arbitrary objects, the drag force experienced by a moving body traveling through a fluid cannot be calculated analytically. Since we wish to quantify our results with theory, we will focus on spherical objects in three dimensions where the Stokes drag is

$$\mathbf{F} = 6\pi\eta a\mathbf{v}. \tag{4.1}$$

This is not a limitation of the algorithm; arbitrary shapes are just as easily implemented. There are still some subtleties in measuring this drag force accurately in a simulation. The first is that the velocity $\mathbf{v}$ in (4.1) is relative to the far-field fluid velocity. If we have a simulation with periodic boundary conditions and introduce a particle moving at a constant velocity, eventually the fluid in the simulation box will "catch up" to the particle (i.e., everything in the box ends up moving with constant velocity). This is a consequence of the Galilean invariance of Navier–Stokes equations.

One way to impose a zero far-field velocity is to break Galilean invariance in our system by introducing walls, as shown in Figure 4.1. As shown, we can either hold the particle still and move the walls (Figure 4.1(a)), or hold the walls still and move the particle (Figure 4.1(b)). It is useful to examine both to ensure the resolution of the underlying fluid mesh does not affect the result. The arrangement of Figure 4.1 reduces finite-size effects ($1/L^2$ instead of $1/L$) [41] and is widely used by experimentalists to measure fluid viscosity with the so-called falling-ball viscometer. Alternatively, we may place a stationary sphere in a shear flow (Figure 4.1(c)), in which case the velocity $\mathbf{v}$ in (4.1) is relative to the velocity the fluid would have at the location of the particle if it were not present (i.e., half of the top wall velocity if the particle is placed halfway between the moving top wall and stationary bottom wall). In this case, the sphere also experiences a drag torque [42] of

$$\mathbf{T} = 4\pi\eta a^3 (v_w/h)\mathbf{n}, \tag{4.2}$$

where v_w is the speed of the top wall, h is the separation of the walls, and $\mathbf{n}$ is a unit vector orthogonal to the shear plane. An additional complication comes from finite-size effects (which are already significantly reduced in the configurations of Figure 4.1). We will address these in more detail below, as they also arise from hydrodynamically induced particle-particle interactions, which are present even in a simulation with only one actual particle as the particle sees its periodic or reflected images through the boundaries.

In the Oseen theory [8] the force from hydrodynamic interactions on identical spherical particles is related to the particle velocities via a mobility tensor $\mathbf{H}$,

$$\mathcal{V} = \mathbf{H}\mathcal{F}, \tag{4.3}$$

where $\mathcal{V} = (\mathbf{v}_1, \ldots, \mathbf{v}_n)$ is a column vector of particle velocities, and $\mathcal{F}$ is a corresponding column vector of the hydrodynamic forces on the particles. The hydrodynamic mobility tensor, also known as the Oseen tensor, has components

$$\mathbf{H}_{ii} = \frac{\mathbf{I}}{6\pi\eta a}; \quad \mathbf{H}_{ij} = \frac{1}{8\pi\eta R_{ij}} \left(\mathbf{I} + \hat{\mathbf{R}}_{ij}\hat{\mathbf{R}}_{ij}\right), \tag{4.4}$$

where a is the radius of the sphere, η is the viscosity of the fluid, $\mathbf{I}$ denotes the 3×3 unit matrix, and $\hat{\mathbf{R}}_{ij}$ is the unit vector parallel to $\mathbf{R}_{ij} = \mathbf{r}_i - \mathbf{r}_j$. We reserve Greek indices for spatial components and Latin indices for particle labels. The Oseen description is based on linearized hydrodynamics and assumes instantaneous propagation of the interactions. As a result, the Oseen drag forces and interactions are valid only in an *intermediate* range of distances [27]. In the time it takes for a particle moving at speed v to move its radius a, the information about its change in location is transmitted a distance

$$L_O = \frac{\eta}{\rho v}, \tag{4.5}$$

and so the interactions should be expected to be modified beyond L_O. However, the correction to the drag on a single particle [27],

$$\mathbf{F} = 6\pi\eta a\mathbf{v}\left(1 + \frac{3}{8}\frac{a}{L_O}\right), \tag{4.6}$$

is small as long as all length scales are smaller than L_O (this includes length scales such as a, R_{ij} and the linear size of our system L). At short range, improvements have been made to (4.4), the simplest being the Rotne–Prager (RP) tensor [9]:

$$\begin{aligned} \mathbf{M}_{ii} &= \frac{\mathbf{I}}{6\pi\eta a}; \\ \mathbf{M}_{ij} &= \frac{1}{8\pi\eta R_{ij}}\left((\mathbf{I} + \hat{\mathbf{R}}_{ij}\hat{\mathbf{R}}_{ij}) + \frac{2a^2}{3R_{ij}^2}(\mathbf{I} - 3\hat{\mathbf{R}}_{ij}\hat{\mathbf{R}}_{ij})\right), \end{aligned} \tag{4.7}$$

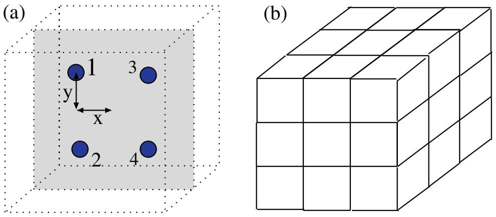

FIG. 4.2. *Setup for the four-particle system.* (a) *The simulation box with four particles placed with their centers at* $(\pm x, \pm y)$ *relative to the center of the box. Particles* 1 *and* 3 *are moved in the* $-y$ *direction at a constant velocity* U_y*, and particles* 2 *and* 4 *are moved with exactly the opposite velocity.* (b) *The nearest periodic images used in* (4.4) *and* (4.7) *with the center box being the simulation box.*

where the additional term of order R^{-3} makes a significant difference to the Oseen tensor only when the two particles are at short distances from each other. The RP tensor gives reasonable results (assuming small Re) down to separations comparable to the particle diameter [43]. Work on Stokesian dynamics has continued to develop [44]. For example, the effect of walls has been studied, which has revealed noteworthy limitations of the Oseen and RP tensors in confinement [45]. Such extensions of Stokesian dynamics are nevertheless technically challenging to implement.

4.2. Quantitative validity of hydrodynamic mobility tensors. As with the Stokes measurement described above, all the velocities in the Oseen or RP description are relative to a far-field velocity that the theory assumes to be zero. To compare our results for the hydrodynamics with the RP and Oseen results, we must ascertain first when the tensor description gives quantitatively correct results. For this, we will make use of the configuration shown in Figure 4.2. This configuration gives us the opportunity to test both hydrodynamic forces parallel to the direction of particle motion (drag) and forces perpendicular to the direction of motion (this requires noncollinearly moving particles). The two sets of two particles in our box are moved in equal and opposite directions to ensure that no net velocity is imparted to the fluid (i.e., to ensure the far-field velocity is zero). Taking torques about the center of mass of the system, it is also clear that this configuration of particles transmits no net vorticity to the fluid, again assuring that the far-field rotational velocity remains zero. All of our simulations are carried out in a finite box, using either periodic or hard-wall boundary conditions. As a result, there is actually an infinite number of periodic or reflected-image particles which must be addressed. To get a feeling for the finite-size effects we include one "shell" of periodic images of our system, as shown in Figure 4.2(b). Analogously to Coulomb interactions, an Ewald-like sum can be performed over the entire set of periodic lattice images [46]. Although this method converges quickly, it is somewhat complicated to implement fully. Further, as images are likely to be at distances considerably greater than L_O, the result does not converge to the solution of the full nonlinear Navier–Stokes equations that are solved by the LB method, but to the solution of the approximate linearized equations. Also, the inclusion of boundaries would require specialized transformations, making the conversion to reciprocal space considerably more difficult. Simply increasing the system size of the simulation box while keeping the particles close to the center of the box is the simplest method for reducing the finite-size effects, although we will keep one shell of periodic images. The farther the periodic images are from the system the less they influence the results obtained.

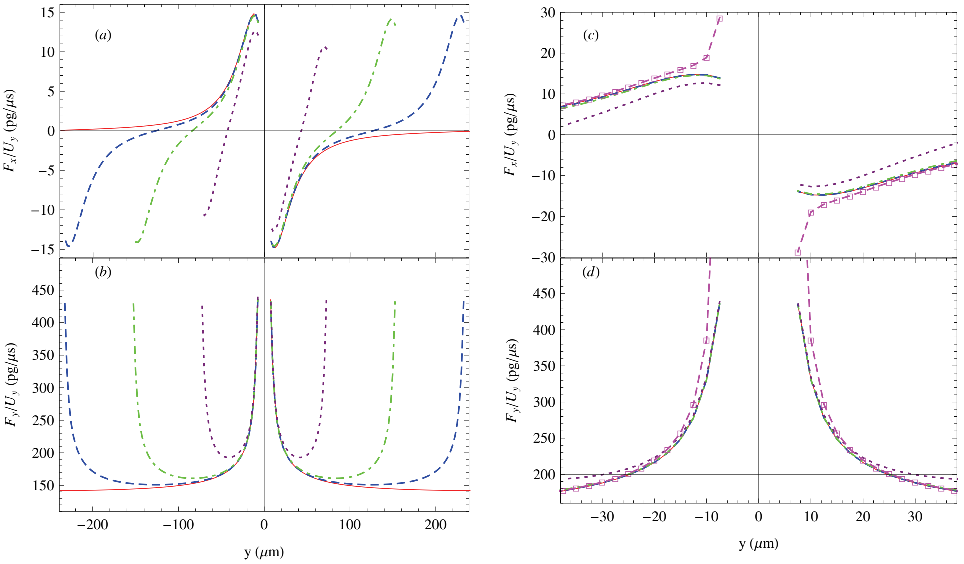

FIG. 4.3. *RP (lines without markers) mobility tensor predictions of forces in the* (a) *x and* (b) *y directions normalized by y-velocity (particles have velocity $\mathbf{v} = (0, \pm U_y, 0)$) on one of four particles in a four-particle system (see text and Figure* 4.2*) designed to test particle-particle interactions. The particle has radius $a = 8\,\mu m$, and the relative x-displacement from the center of the box is $x = 24\,\mu m$. Different lines refer to different system sizes (distance to periodic images) of $L = 160\,\mu m$ (dotted), $320\,\mu m$ (dot-dashed), $480\,\mu m$ (dashed), and $960\,\mu m$ (solid). Graphs* (c) *and* (d) *are blow-ups of the central region in* (a) *and* (b)*, respectively, and they also show the Oseen prediction for the largest system (dashed line with hollow square markers). There is good agreement between the RP results in the central region for $L \geq 320\,\mu m$. The $L = 160\,\mu m$ is too small a system in the sense that the image charges are too close to each other, affecting the results even in the central region. The origin is at the center of the box.*

To quantify the finite-size effects, we examine the Oseen and RP predictions for a system of four spheres, as described in Figure 4.2, where $a = 8\,\mu$m, $x = 24\,\mu$m, and particles 1 and 3 move in the $-y$ direction at a speed of $U_y = 0.0025\,\mu$m/μs and particles 2 and 4 move in the $+y$ direction with the same speed. The predictions for system sizes L from $160\,\mu$m to $960\,\mu$m are shown in Figure 4.3. We emphasize that these are the RP predictions, not results from our algorithm. It is clear from Figure 4.3(a) that as the particle approaches the edge of the box, the force F_x on it differs significantly as L increases. However, the change in the central region, i.e., $-40\,\mu$m $< y <$ $40\,\mu$m, of the box is much smaller and, as shown in Figure 4.3(c) and (d), there the difference is less than 0.25% for $L \geq 320\,\mu$m. Thus, to compare these findings directly with our LB simulations, we will use a system size of $320\,\mu$m and restrict our particles to the central region of $-40\,\mu$m $< y <$ $40\,\mu$m, where the RP tensor gives quantitative results with only small finite-size effects. It is easy to see from Figure 4.3(c) and (d) the unphysical increase in the transverse force in the Oseen results but not in the RP results as the gap between the particles decreases. As such we will use the RP mobility in all calculations below.

5. Results. We first examine the hydrodynamic drag and torque experienced by a single particle as a function of the bare coupling to the fluid γ. Particle-particle interactions are then studied. Finally, the diffusive properties of a single particle are examined. Each of these tests can be used to define a “hydrodynamic” radius. As

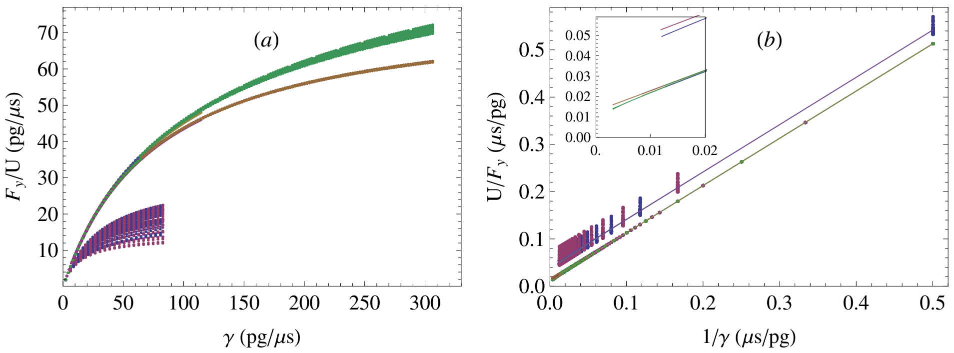

FIG. 5.1. (a) *Drag force divided by velocity* (F_y/U) *as a function of the fluid-particle coupling* γ *for point particles in systems of sizes* $L = 35$, 50, *and* $80\,\Delta x$. *The top pair of curves uses the Peskin (P) stencil for the force, with the the lower of the two using Peskin-interpolated (P) fluid velocity and the upper curve using site velocities (cf.* (5.2)*). The results in the Peskin case overlap for different system sizes, and only the* $L = 50\,\Delta x$ *data are shown for the full range of* γ*, i.e., beyond* $\gamma = 120\,\mathrm{pg}/\mu\mathrm{s}$*, for clarity. The lower pair of curves plotted up to* $\gamma \approx 85\,\mathrm{pg}/\mu\mathrm{s}$ *uses the trilinear (T) stencil for the force (blue is noninterpolated and purple is T-interpolated velocity; color is available only in the online version) in an* $L = 50\,\Delta x$ *system. The T-stencil is numerically unstable for larger gamma. The vertical smearing, most prominent for the trilinear stencil, is a result of mesh effects (see text).* (b) *Inverse of the data plotted in* (a). *The lines in* (b) *are from averaging the data at a given* γ *over the different positions in a cell of the fluid mesh.*

such, they constitute a consistency check, and as we will see they do not necessarily give consistent results. We then show how particles can be constructed in a way so as to yield reasonably consistent results for all these tests.

5.1. Point particle. The smallest particle one can use consists of a single node, a point particle, so it is worth examining this case first. Such particles have been used in works with thermal noise [24, 25, 47]. The first setup measures Stokes drag and is shown in Figure 4.1(a) and (b). There are two possible configurations, one where the walls are moving at constant velocity and one where the particle moves at constant velocity with the walls fixed. The two situations are made equal by Galilean invariance, so they should give the same steady state force on the particle. However, we used the second case (particle moving with an average speed of U and the magnitude F_y of the force measured using (3.13)), as it highlights the effect of the underlying fluid mesh. Also, we added a small ($\pm 0.5\,\Delta x$) sinusoidal variation in the particle's trajectory, with a period equal to the linear box size, in the direction perpendicular to the average direction of motion so that the particle samples many positions relative to the fluid mesh. For these runs, $\Delta x = 4\,\mu\mathrm{m}$, $\Delta t = 4\,\mu\mathrm{s}$, and $\tau = 0.75\Delta t$. We repeated the experiment for many different values of γ in order to measure the drag force as a function of γ. We performed the measurement in systems of linear sizes $L = 35\Delta x$, $50\Delta x$, and $80\Delta x$ (i.e., the simulation box was $L \times L \times L$), and the results are shown in Figure 5.1. The first observation is that the results from all system sizes are indistinguishable on this plot. Finite-size effects can be measured and do scale like $1/L^2$, as is expected in this geometry (the presence of the walls changes the finite-size effects from $1/L$ to $1/L^2$; see [41]), but in this case they are too small to be a concern. This is a huge advantage over previously suggested means of calibrating the value of γ.

As is obvious from Figure 5.1(b), our data follows the relationship also seen

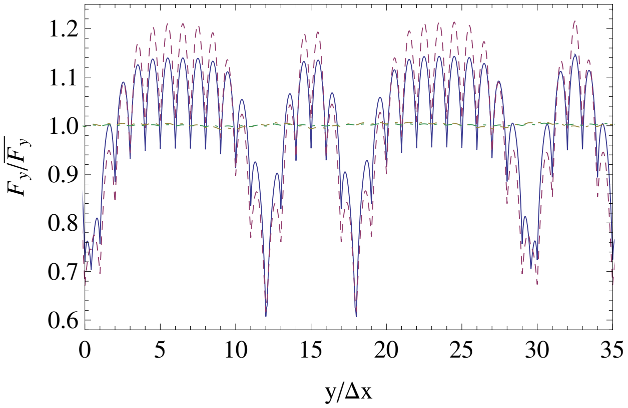

FIG. 5.2. *Drag force normalized by its mean as a function of particle position for a system of linear size* $L = 35\,\Delta x$ $(\Delta x = 4\,\mu m)$. *The solid line is the trilinear stencil without interpolation, the dashed line is the trilinear stencil with interpolation, and the dot-dashed line uses the Peskin stencil.*

in [24, 25] that the inverse drag coefficient is a linear function of $1/\gamma$:

$$U/F_y = 1/\gamma_I + 1/\gamma, \tag{5.1}$$

where $1/\gamma_I$ a constant realized in the limit $\gamma \to \infty$. However, as shown in the inset of Figure 5.1(b) for the noninterpolated velocity $\hat{\mathbf{u}}_i = \hat{\mathbf{u}}(\mathbf{x}_j)$, namely

$$\mathbf{F}_{ij} = (\mathbf{v}_i - \hat{\mathbf{u}}(\mathbf{x}_j))\xi_{ij}\gamma, \tag{5.2}$$

the measured force-$1/\gamma$ relation deviates from the linear relationship slightly for large values of γ. While this deviation seems very small on the inverse plots (it is not even visible in the main plot of Figure 5.1(b)), it actually leads to very significant deviations ($\sim 15\%$) in the drag force, as manifested by the difference between the Peskin-interpolated velocity and noninterpolated velocity results in Figure 5.1(a) at $\gamma = 300\,\mathrm{pg}\,\mu\mathrm{s}^{-1}$. Another prominent feature of Figure 5.1 is the vertical smearing of the forces due to lattice effects, particularly noticeable for the trilinear stencil. The lattice effect is illustrated in Figure 5.2, which shows the drag force versus position for a particle moving over the lattice. The lattice effects for the Peskin stencil are negligible, but those for the trilinear stencil lead to fluctuations of roughly 30% about the mean. Note also that the use of interpolated velocity in (3.8) makes little difference to the lattice effects. The small difference between the noninterpolated and the interpolated velocities stems from (5.2). The summation of the expression over the affected mesh sites leads to

$$\sum_j \mathbf{F}_{ij} = \left(\mathbf{v}_i - \sum_j \hat{\mathbf{u}}(\mathbf{x}_j)\xi_{ij}\right)\gamma \tag{5.3}$$

due to (3.7). The sum on the right-hand side is, by definition, the interpolated velocity. The scale of these lattice effects suggests that using the trilinear stencil for point particles is questionable. However, Ahlrichs and Dünweg [24, 25] did use a similar scheme for polymers consisting of point particles and did not report any adverse affects. This may be due to some averaging out of the mesh effects for spatially extended objects, as long as the spacing between nodes is not commensurate with the lattice mesh. However, the polymer dynamics could be affected by these mesh effects, and it would be hard to know a priori if this were the case [48].

The intercept of Figure 5.1(b) in the limit $\gamma \to \infty$ can be used to define an "intrinsic" size a_I,

$$a_I = \frac{\gamma_I}{6\pi\eta}. \tag{5.4}$$

For the Peskin stencil with velocity interpolation, the intercept $1/\gamma_I$ in this case is $0.013\,\mu\text{s}\,\text{pg}^{-1}$, which corresponds to a value of $a_I = 4.08\,\mu\text{m} = 1.02\,\Delta x$. This corresponds to the *largest* possible "hydrodynamic radius" in the limit of infinite γ that a Peskin point particle could have. Its proximity to Δx is interesting in that the Peskin compact support is $\pm 2\Delta x$, so this is smaller than what one might have naively thought to be the potential maximum. For the trilinear stencil the intercept is $0.036\,\mu\text{s}\,\text{pg}^{-1}$ without interpolation in the velocity which corresponds to $a_I = 1.47\,\mu\text{m} = 0.37\,\Delta x$. Thus, the trilinear stencil will always give rise to a smaller effective size. In [24, 25], having fixed γ based on a desired diffusion coefficient, it was suggested to assign a hydrodynamic radius to the point particle by equating it to $a_h = F_y(\gamma)/(6\pi\eta U)$, the Stokes drag on a sphere of radius a_h. Doing this allowed them to use any value of γ, and, in particular, rather small values that did not lead to numerical instabilities. However, as we will show below, there are several ways to define a hydrodynamic radius, and defining it as $F_y(\gamma)/(6\pi\eta U)$ for an arbitrary value γ does not lead to consistent results. Perhaps a more serious problem with the trilinear stencil is the existence of mesh effects. We will first examine composite particles with the goal of reducing them. One might question why we do not simply abandon the trilinear stencil altogether and use the Peskin stencil, as mesh effects are almost absent. The reason is that the Peskin stencil has the very serious disadvantage of extending more than one lattice site from its center, which can lead to problems near boundaries, and requires a scan over 64 lattice sites rather than 8 in three dimensions, so it is more costly to compute.

5.2. Composite particle. Mesh effects can be greatly reduced by using composite particles (with each node projected onto the fluid mesh using a trilinear stencil) like those in Figure 3.2. The first decision in using such a particle is on the number N_v of surface nodes (i.e., the resolution relative to the fluid mesh). It seems clear that if one wants the sphere to be impermeable, the nodes on the sphere ought to be closer than Δx apart. However, it is not clear beforehand how much closer is necessary. Figure 5.3 shows the drag force on a subgrid composite particle of radius $a = 0.6\,\Delta x$ for fullerenes with different N_v, where a is the radius at which the nodes in the fullerene sit, as a function of the drag coefficient γ scaled by the total number N_v of nodes on the sphere. It is evident that the composite particles, even with a subgrid radius, have greatly reduced mesh oscillations (about 10% for 30 nodes and less than 3% for a few hundred nodes, rather than the 30% found for the point particles; cf. Figure 5.1). This makes a trilinear stencil (for a particle comprised of 60 or more nodes) a potential alternative to the Peskin point particles for subgrid resolution. There is no saving in computing time here, however, as we will have $8N_v$ points in the effective stencil for the entire particle. There may still be an advantage to using such particles since they have a smaller compact support on the fluid mesh (i.e., the stencil extends only one lattice site away from the particle, unlike the Peskin stencil, which extends two lattice sites), which is favorable particularly at boundaries. For larger composite particles the mesh effects are even smaller and hardly visible (i.e., similar to Peskin) for composites of radius $2\Delta x$ or larger.

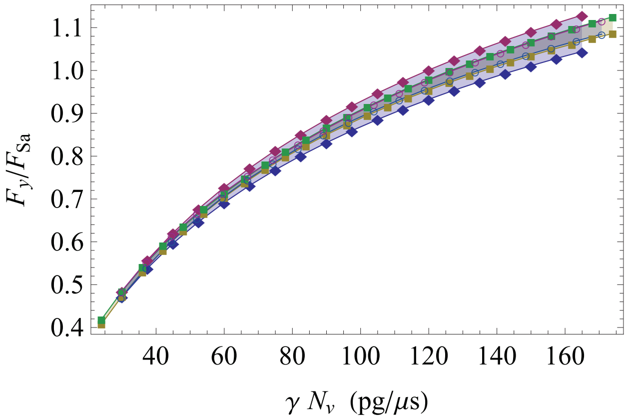

Fig. 5.3. *Drag force on a composite particle sphere of radius $a = 0.6\Delta x$ normalized by the expected Stokes drag on such a sphere. The lines are upper/lower bounds for mesh oscillations of the drag force as the particle moves over the underlying fluid mesh. Diamonds denote bounds for mesh oscillations for a sphere with* 30 *nodes, squares are bounds for a sphere with* 240 *nodes, and open circles are bounds for a sphere with* 2970 *nodes (each node is projected onto the fluid mesh using a trilinear stencil).*

By measuring simultaneously the drag force and torque on a particle in shear flow, we have two means of defining a hydrodynamic radius. The first makes use of (4.1),

$$a_{h,F} = F_y/(6\pi\eta U), \tag{5.5}$$

where U is the velocity at the particle location (i.e., half of the upper wall velocity in Figure 4.1(c)). As mentioned above, this was used to assign a hydrodynamic radius to point particles (eq. (19) and below in [24, 25]) and to composite particles (eq. (30) and below in [39, 40]), the implicit assumption being that any reasonable way of defining a hydrodynamic radius should give a similar result. Alternatively, one can make use of (4.2) for the torque,

$$a_{h,T} = \left[T_z/(4\pi\eta v_w/h)\right]^{1/3}. \tag{5.6}$$

These different measures for the hydrodynamic radius, including a separate run to measure drag force using the protocol of Figure 4.1(b), are shown in Figure 5.4. We see that the two different protocols for measuring the hydrodynamic radius from the drag force give consistent results. However, the hydrodynamic radius calculated from the torque gives results very different from that based on the drag force, except when γ is very large. Obviously, an infinite γ is not a feasible option, so the relevant question is how large γ needs to be for the torque and drag force to give consistent results in imposing the effective no-slip boundary condition on the surface of the sphere. For the system in Figure 5.4, we found that if γ is large enough so that $a_{h,F}$ as defined by the drag force is within 1% of the radius expected from the nodes comprising the sphere ($a = 2\,\Delta x$ here), then the $a_{h,T}$ defined by the torque is also within 1% of this radius (although it disagrees with the drag force radius by 2%). Agreement improves as one increases γ as a_h approaches an intrinsic size (intercept in Figure 5.4), which is consistent with the point particle intrinsic size (i.e., $a_h \to a + a_I$, where a_I is the intrinsic size of a point particle discussed above). The Peskin stencil yields

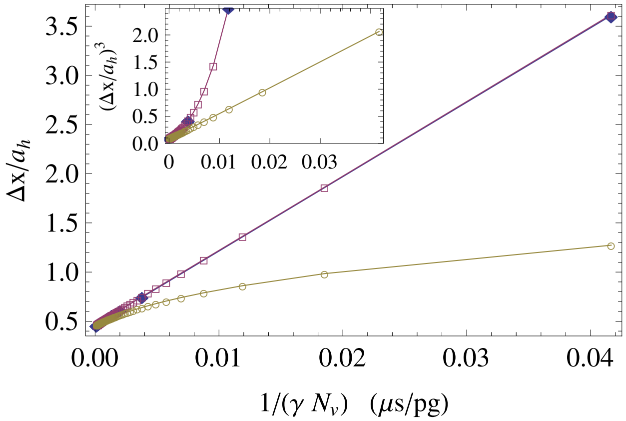

FIG. 5.4. *Inverse of hydrodynamic radius measured from drag forces and torques on a composite particle sphere of radius* $a = 2.0\,\Delta x$. *Solid diamonds are hydrodynamic radius as computed by drag force on a moving sphere (Figure* 4.1(b)*), open squares are hydrodynamic radius as computed by drag force on a fixed particle in a shear flow (Figure* 4.1(c)*), and open circles are hydrodynamic radius as computed by drag torque on a fixed particle in a shear flow (Figure* 4.1(c)*). All results use trilinear stencil and interpolated velocities at the nodes. This demonstrates that* $1/a_h$ *measured from drag forces is a linear function of* $1/\gamma$, *whereas the same quantity from drag torque is not. Inset: Inverse of hydrodynamic radius cubed versus* $1/(\gamma N_v)$ *showing that* $1/a_h^3$ *from the torque shows a linear relationship.*

very similar results, although a_I is larger for the Peskin stencil, so a large enough γ is needed so that a_h will be slightly larger than a in order to get the same level of agreement in a_h from torque and force measurements. The main caveat is that consistency was achieved only when the interpolated velocity was used for $\hat{\mathbf{u}}$ in (3.8). When the noninterpolated velocity was used, the $\gamma \to \infty$ limit did not give consistent results for the torque and force measurements ($a_{h,T}$ from torque was always larger than $a_{h,F}$). This is due to the property of (5.3), as the use of noninterpolated velocity distributes the force farther from the particle center, thereby adding to the torque. As a result, we will use only interpolated velocities in the remainder of this work.

In some situations, it may be reasonable to ignore torques, so one might ask whether it is then permissible to use just (5.5) to define a hydrodynamic radius, as was done in [24, 25] for point particles. This is not the case for composite particles, such as those of Figure 3.2, as it should be fairly obvious that γ needs to be large enough so that the drag force on the composite sphere results in a hydrodynamic radius, as defined by (5.5), that is, at least as large as the radius at which the individual nodes are centered. If this were not the case, one might have the perverse expectation that the hydrodynamic interaction between two particles would not show the $1/r$ divergence expected from Oseen or RP theories until the nodes making up the composite particles were actually overlapping. However, if γ is large enough to produce the drag force expected for a particle with nodes sitting at a distance a, then consistency with the torque will be quite reasonable, as discussed above.

For subgrid size composite or point particles it would still be desirable to use (5.5) to define a hydrodynamic radius. We examine the hydrodynamic interactions for this case. We compare a point particle (with Peskin stencil) and a composite particle (with nodes mapped using the trilinear stencil) with γ chosen to give a hydrodynamic radius of $a_h = 0.475\,\Delta x$ (as defined by (5.5) using the configuration of Figure 4.1(a)).

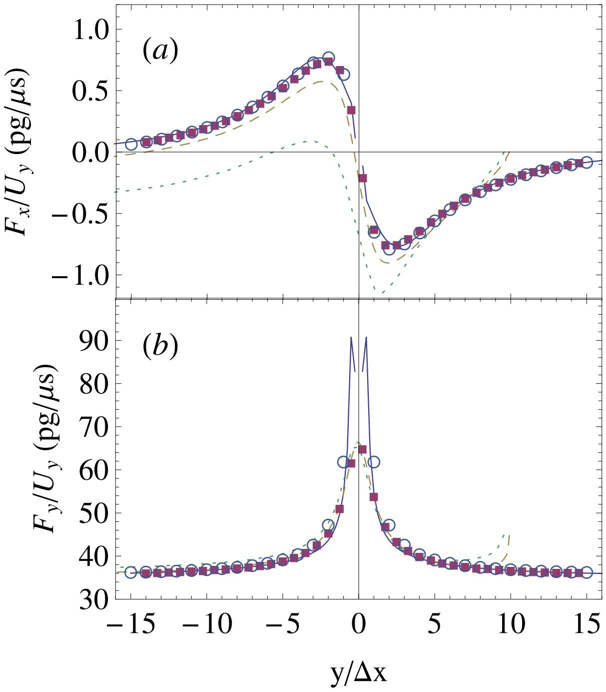

FIG. 5.5. *Forces normalized by y-velocity (particles have velocity* $\mathbf{v} = (0, \pm U_y, 0)$*) on one of four particles in a four-particle system (see text) designed to test particle-particle interactions. The solid line is the result from the RP tensor for particles of size* $a = 0.475\,\Delta x$*. Other lines and the solid squares are from simulations using Peskin point particles with* γ *set to give a hydrodynamic radius* a_h *of* (5.5) *equal to* $a_h = 0.475\,\Delta x$*. The dotted line corresponds to particle speed* $U_y = 0.05\,\Delta x/\Delta t$*, the dashed to* $U_y = 0.01\,\Delta x/\Delta t$*, and the solid squares to* $U_y = 0.0005\,\Delta x/\Delta t$*. The open circles are from simulations using composite particles with trilinear stencil with node radius* $a = 0.475\,\Delta x$ *and* γ *tuned to give* $a_h = a$*. Note the effect of the finite propagation speed causes an asymmetric lag compared to the RP result when the particles are moving quickly, most noticeable in the lift* (F_x) *near its maxima. This lag is no longer visible for more slowly moving particles with* $U_y = 0.0005\,\Delta x/\Delta t$*.*

We then put four particles in the configuration of Figure 4.2(a) and measure the forces on one of the four particles. The result is shown in Figure 5.5. Note that there are *no fitting parameters* here and the results are quantitatively matching for small enough velocities consistent with the investigations of section 4.2. In these runs, we made the particles pass through each other in order to explore the full possible range of the hydrodynamic forces. In normal use, one would add some sort of hard sphere interaction between the particles to prevent overlaps. The first thing to note is the comparison between the faster moving Peskin stencils ($U_y = 0.001\,\Delta x/\Delta t$ and $0.05\,\Delta x/\Delta t$) versus the slower one ($U_y = 0.0005\,\Delta x/\Delta t$). For the faster particles (the dotted and dashed lines), we also show the start-up period (system was started with the fluid in a quiescent state), and we see that the particle moves a distance comparable to its diameter before the forces coincide with the expectation from the RP tensor, which assumes instantaneous equilibration. Looking at the force perpendicular to the particle velocity, F_x, as the particles approach each other we can also see a significant asymmetric lag compared to the RP result for the faster moving particles. This is a consequence of the finite propagation speed of fluid-mediated interactions and the fact that as the particles approach each other, the force is changing very rapidly.

This asymmetric lag is no longer visible for particles moving with $U_y = 0.0005\,\Delta x/\Delta t$ (○, ■). It is interesting that the lag is so significant for particles very close to each other, as our original expectation was that finite propagation times would have an impact only at large separations. This could have an impact in shear flows of dense colloidal suspensions. Not surprisingly, the force does not diverge as the particles approach (and overlap), contrary to what is expected from the Oseen prediction. The forces do, however, get very large, so these Oseen-like interactions should work well for dilute systems where particles are not packed tightly against each other but may collide momentarily. The one caveat is that the peak in the measured F_y is slightly wider than what would be expected for a particle of this size. This is not that surprising considering the observations above that the intrinsic size a_I of a Peskin stencil point particle is about Δx and the intrinsic size of the trilinear stencil ($\sim \Delta x/3$) makes it larger than the radius a at which the nodes in the composite particle sit.

Finally, it is worth considering that once one has calibrated a system with a sphere of a given size, how does one use this information for a sphere of different size or for a soft sphere where the bond lengths in the fullerene are not fixed? What we have found is that the key quantity that must be constant is the ratio of γ to the area per node A_n,

$$\text{constant} = \frac{\gamma}{A_n} = \frac{\gamma N_v}{4\pi a^2}. \tag{5.7}$$

That is, if one calibrates for a sphere of radius a and then wants to change to a sphere of radius $2a$, then one should scale γ by 4. However, the larger sphere will need more nodes (nodes need to be closer than Δx apart), so, in this example, one could keep γ constant and multiply N_v by four to get the larger sphere calibrated. Unfortunately, there is a small dependence of the intrinsic size a_I on the time step Δt so that if one changes Δt, one may need to recalibrate γ to give the correct drag. Similar effects are found using the standard bounce-back scheme for flat walls, for which the location where the velocity can be extrapolated to zero can change slightly as a function of τ.

From an efficiency standpoint one may try to use as few nodes as possible, as long as mesh effects such as the oscillations in Figure 5.3 are below a tolerable level. Generally, nodes need to be closer than Δx apart for both trilinear and Peskin stencils, but there is almost no advantage seen for nodes spaced closer than about $\Delta x/4$ apart for a trilinear stencil and $\Delta x/2$ apart for a Peskin stencil (typically less than 1% difference for closer spacings; cf. Figure 5.3). The Peskin stencil has somewhat better numerical stability than the trilinear stencil (cf. Figure 5.1) and requires fewer nodes; however, it has eight times as many points per node. The trilinear stencil is a viable option in systems with walls, as its support extends only one lattice site from each node. The trilinear stencil also makes it feasible to simulate subgrid size particles down to $0.6\,\Delta x$, which would have a larger radius if the Peskin stencil were used due to its larger intrinsic radius.

5.3. Diffusion of point and composite particles.

Having achieved criteria for consistency of the hydrodynamic radius through deterministic tests of solute particles we now turn to the subtle issue of thermal noise in the LB methodology. Common hybrid algorithms [24, 25, 15, 16, 39, 40] that mix LB and MD operate in a regime where thermal noise is important and use a Langevin equation for the nodes, which is of the form

$$\begin{aligned} m\,\mathrm{d}\mathbf{v}_i/\mathrm{d}t &= -\gamma(\mathbf{v}_i - \hat{\mathbf{u}}_i) + \mathbf{F}_{R,i}; \\ \langle F^{\alpha}_{R,i}(t)\rangle &= 0; \\ \langle F^{\alpha}_{R,i}(t)F^{\beta}_{R,j}(t')\rangle &= 2\gamma k_{\mathrm{B}}T\delta(t-t')\delta_{\alpha\beta}\delta_{ij}, \end{aligned} \tag{5.8}$$

where $\alpha, \beta \in \{x, y, z\}$, i and j run through the node indices, $\mathbf{v}_i$ is the velocity of a node, and $\hat{\mathbf{u}}_i$ is the interpolated fluctuating fluid velocity at the node's location. Thermal fluctuations are present in (5.8) in both the fluid velocity $\mathbf{u}$ according to fluctuating hydrodynamics [27] and in $\mathbf{F}_R$. If the particle is an extended rigid object, a similar equation for rotational degrees of freedom is also used. In (5.8), the amplitude of the random force diverges as the coupling constant $\gamma \to \infty$, which is clearly undesirable if one wishes to approach the no-slip limit. Moreover, as $\gamma \to \infty$ and $-\mathbf{F}_R$ is applied locally to the fluid to conserve momentum, the hydrodynamic correlations between particles are ultimately overpowered by $-\mathbf{F}_R$, which is uncorrelated in both space and time. This is very different from the common use of Langevin dynamics, say, as a thermostat in MD, where γ is deliberately chosen to be small enough to minimize impact on physically relevant processes, such as dissipation from viscous shear in a fluid.

Although not widely acknowledged, it has been proven explicitly that Langevin noise $\mathbf{F}_R$ as in (5.8) is not needed for the coupled particle-fluid system to obey a fluctuation-dissipation theorem *in the no-slip limit* [49]. In the preceding sections, we have shown our LB algorithm to recover the no-slip limit for Stokes drag, for drag torque, and for particle-particle interactions at zero temperature without any fitting parameters as we approach the limit $\gamma \to \infty$ numerically. In this section, we investigate the level of dissipation in simulation when the choice of the key algorithmic parameter γ is made to guarantee impermeability and the no-slip boundary condition according to the criteria we have outlined above.

In view of the available theory [49] and our calibration procedure, the role of $\mathbf{F}_R$ in (5.8) clearly merits comment. We address this question in the context of an equation of motion without external Langevin noise, i.e.,

$$m\,\mathrm{d}\mathbf{v}_i/\mathrm{d}t = -\gamma(\mathbf{v}_i - \hat{\mathbf{u}}_i), \tag{5.9}$$

in which the fluctuating fluid velocity $\hat{\mathbf{u}}_i$ is the only source of fluctuations for the node. We emphasize that in contrast to common folklore, there is no fundamental theoretic flaw in leaving out $\mathbf{F}_R$ *in the no-slip limit* [49]. We begin our argument by considering the rate of change of kinetic energy of a node, S_i, which can be written as

$$S_i \equiv \frac{\mathrm{d}}{\mathrm{d}t}\left(\frac{1}{2}m\mathbf{v}_i^2\right) = m\mathbf{v}_i \cdot \frac{\mathrm{d}\mathbf{v}_i}{\mathrm{d}t} = -\gamma\mathbf{v}_i \cdot (\mathbf{v}_i - \hat{\mathbf{u}}_i), \tag{5.10}$$

where the last equality follows from (5.9). We plot the measured average total dissipation, $\langle S\rangle = \langle\sum_i S_i\rangle$, as a function of the algorithmic parameter γ in Figure 5.6 for a freely diffusing (translationally and rotationally) spherical shell consisting of $N_v = 240$ nodes. Thermal fluctuations are present in the LB fluid, as detailed in [23], *without any Langevin noise on the particle*. Figure 5.6 tells us that the dissipation is a bounded function that first increases and then *drops* as γ is increased. The no-slip limit and consistency between different deterministic measures is attained around 48 ag/ns for all practical purposes. In general, to achieve the no-slip limit we find

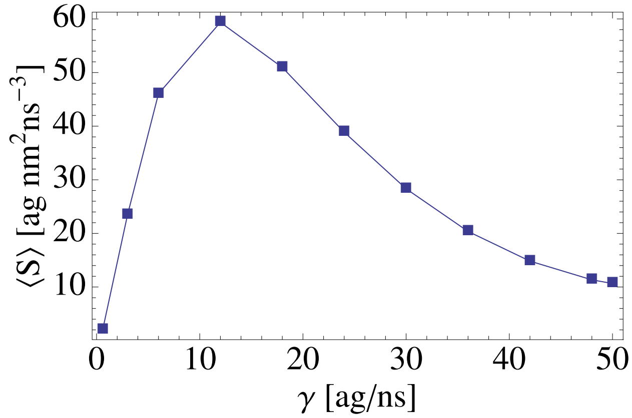

FIG. 5.6. *Rate of dissipation of kinetic energy* $\langle S \rangle$ *of a* 240*-node shell is a bounded function of the coupling constant* γ*.* $\langle S \rangle$ *at saturation (*$\gamma > 48\,\mathrm{ag/ns}$*) is less than* 0.01% *of the rate of dissipation present in the fluid at the scale of the particle in the absence of the particle. The lines between data points are there to guide the eye. The particle radius is* $R = 2.0\,\Delta x = 20\,\mathrm{nm}$.

that γ must be set to a value that forces a mass of $\rho \Delta x^3 / N_v$ to relax in a time scale of the order of a time step Δt. The level of dissipation of kinetic energy should be compared to that present in the fluctuating fluid at the scale of the particle in its absence, which may be evaluated as a volume fraction V_{Sphere}/V of the total dissipation $D(\mathbf{u},\mathbf{u})$ [49, 27],

$$D(\mathbf{u},\mathbf{u}) \equiv \int_V \eta \left(\frac{\partial u_\alpha}{\partial x_\beta} \frac{\partial u_\alpha}{\partial x_\beta} + \frac{\partial u_\alpha}{\partial x_\beta} \frac{\partial u_\beta}{\partial x_\alpha} \right) \mathrm{d}V. \tag{5.11}$$

We find a level of dissipation of 1.2×10^5 ag nm^2 ns^{-3} to be present at the scale of the particle, which is much greater (by orders of magnitude) than the particle dissipation seen in Figure 5.6. This means that *the presence of the particle causes no significant perturbation on the temperature of the fluid*, and corresponding values of the coupling constant γ are fully acceptable.

Whether the dissipation has an effect on the temperature of the particle can be resolved by investigating the velocity autocorrelation function $\mathrm{VACF}(t) \equiv (1/3)\langle \mathbf{v}(t) \cdot \mathbf{v}(0) \rangle$ of the particle. The zero-time limit is known from equipartition to be $\mathrm{VACF}(0) = k_{\mathrm{B}}T/M$, where M is the sum of the mass used to construct the particle and the mass of the fluid within its hydrodynamic radius a_h that necessarily always tracks it. At short times, $t < t_s \equiv a_h/v_s$ (v_s is the speed of sound), compressibility effects are observable in that sound waves transport momentum from the particle and VACF decays from $k_{\mathrm{B}}T/M$ to $\mathrm{VACF}(t_s) = k_{\mathrm{B}}T/M^*$, where $M^* = M + 2\pi a_h^3 \rho/3$ in an incompressible fluid [50]. At long times, compressibility becomes unimportant as sound waves are damped and the incompressible Navier–Stokes equations may be used to predict the asymptotic long-time power-law tail [50, 51, 49] $C(t) = k_{\mathrm{B}}T(12\rho\sqrt{\pi^3\nu^3})^{-1}t^{-3/2}$, where $\nu = \eta/\rho$ is again the kinematic viscosity. We note that $C(t)$ is the same for both the slip and the no-slip boundary conditions [49], so the tail alone tells nothing about the correctness of hydrodynamic interactions. Similar to Iwashita, Nakayama, and Yamamoto [51], we also consider a particle in a thermally quiescent fluid (at $T = 0$) dragged with a constant force F_0 at times $t < 0$ to a steady state and let go by setting $F_0 = 0$ for $t \geq 0$, after which the fluid and the particle relax to a completely quiescent state. Walls far from the particle are needed parallel to the direction of motion to

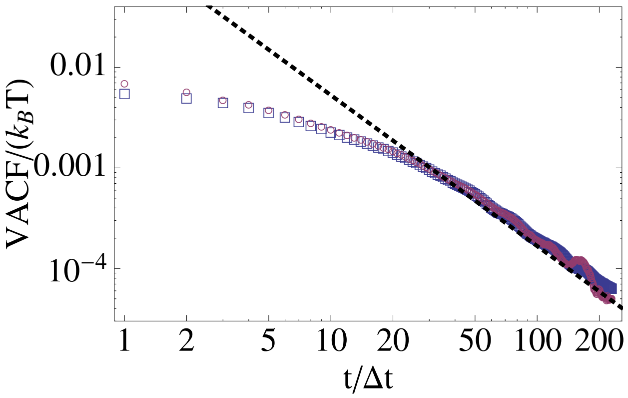

Fig. 5.7. *VACF of a particle diffusing in a fluctuating fluid (circles) and the rate of decay of the velocity of a particle that was in steady state motion due to a constant force* F_0 *for* $t < 0$ *and then relaxes to a quiescent state when the force is removed for* $t > 0$ *in a LB fluid with no thermal fluctuations (squares). The dotted line is the asymptotic long-time power-law tail,* $k_\mathrm{B}T(12\rho\sqrt{\pi^3\nu^3})^{-1}t^{-3/2}$*, divided by* $k_\mathrm{B}T$ [51].

prevent the whole fluid phase from attaining the particle velocity. The deterministic particle has $\mathrm{VACF}(0) = k_\mathrm{B}T/M^*$, as no sound waves are associated with the steady state, nor are they emitted due to deceleration from the steady state. For $t > t_s$, the normalized deterministic deceleration $(-1/F_0)\mathrm{d}v/\mathrm{d}t$ and the normalized correlation function $\mathrm{VACF}(t)/k_\mathrm{B}T$ for the translationally and rotationally freely diffusing particle should be equal [51] in the linear response regime. If this is proven to be the case, and the aforementioned connections between M, M^*, t_s, and R_H are observed as well, then we may confidently state our model to obey the fluctuation-dissipation theorem. We note that the coupling of (5.9) in the no-slip limit effectively removes degrees of freedom, for which reason the mass M^* of the particle is that of the composite particle–dragged fluid object as measured from the zero-time intercept of the normalized deceleration of the deterministic particle (i.e., measured in the absence of noise).

We conclusively establish our particle to obey the fluctuation-dissipation theorem in Figure 5.7. The calculated sound time t_s equals $2.7\Delta x/(\Delta x/\sqrt{3}\Delta t) \approx 4.7\Delta t$ for our particle that has a hydrodynamic radius of $a_h = 2.7\Delta x$, which is congruous with the the data points being on top of each other at $t = 5\Delta t$ in Figure 5.7. We compute the difference $\Delta M = M^* - M$ to be 40 ag from the measured zero-time intercepts $1/M^*$ and $1/M$ of the deterministic and stochastic response functions. By equating the difference with $(2/3)\pi\rho a_h^3$ [50], we find $a_h \approx 2.7\Delta x$ ($\Delta x = 10\,\mathrm{nm}$), which matches with the deterministically measured hydrodynamic radius. Moreover, the mass of the nodes used to construct the particle (66.9 ag) and the fluid contained within its hydrodynamic radius $(4/3)\pi\rho a_h^3 = 82.3\,\mathrm{ag}$ together predict $M = 149\,\mathrm{ag}$, which is very close to the 150 ag measured from the intercept $1/M$. Ergo, we conclude that both equipartition and the fluctuation-dissipation theorem for the particle are obeyed when γ is chosen consistently, as described in the previous sections.

Measuring the diffusion coefficient has been used in the past as a test of polymer dynamics in an LB solvent [24, 25, 52, 23]. This requires thermal noise to be present in some way. These earlier schemes gave reasonable scaling behavior [24, 25] with thermal noise incorporated in the LB scheme as described in [53, 54], but the local temperature fluctuations were often not necessarily correct, as earlier thermal schemes did not give convergence at short wavelengths [53, 54, 22]. That is, full hydrodynamic equations and noise converged to expected values only in the long-wavelength limit, a scale often larger than the characteristic size of colloidal particles of interest [22]. More recent thermal schemes give better thermal noise at short wavelengths [22] as long as $v_s^2 = (1/3)(\Delta x^2/\Delta t^2)$. Our implementation of thermal noise is described in [23]. We approach the topic of the LB fluid functioning as a heat bath and consider the equation of motion of the center of mass velocity $\mathbf{v}$ of our particle with the force being equal and opposite to the fluid force, given by (3.8) and summed over the fluid sites:

$$m\,\mathrm{d}\mathbf{v}/\mathrm{d}t = -\gamma(\mathbf{v} - \hat{\mathbf{u}}). \tag{5.12}$$

The mass m in (5.12) is that of the nodes used to construct the shell. Note that there will be an added mass contribution to this leading to M and M^*, as explained above. Therefore, the mass of the particle is a derived quantity in these systems. Again, we emphasize that the fluctuating fluid velocity $\hat{\mathbf{u}}$ is the *source* of thermal noise as far as the particle is concerned.

For diffusion measurements, we restrict ourselves to the case where $\langle\hat{\mathbf{u}}\rangle = 0$. Far from the particle, the fluctuating fluid velocity obeys the equipartition relation $\langle\hat{u}_\alpha\hat{u}_\beta\rangle = k_BT/(\rho C_v)\,\delta_{\alpha\beta}$, where C_v is the effective volume over which $\hat{\mathbf{u}}$ is averaged (which in the simulation depends on the particular choice of stencil and the number of nodes making up the particle). The desired goal is to obey the fluctuation-dissipation theorem, which tells us that the diffusion coefficient should be related to the ratio of temperature to drag coefficient,

$$D = \frac{k_BT}{6\pi\eta a_h}, \tag{5.13}$$

where a_h is the hydrodynamic radius as determined from one of the measurements described above.

To measure diffusion from our simulations we place a single particle in a cubic simulation box with periodic boundary conditions in all directions. Thermal noise is present, as detailed in [23], which gives rise to velocity fluctuations in the fluid, and particles follow this motion via (5.12). We use a value of $\gamma = \gamma_s$ that gives consistency between the measures of hydrodynamic radius a_h determined in the previous subsection, i.e., consistent drag force and torque. We will use interpolation (see (3.9)) in all cases. To measure the tracer diffusion coefficient of the solute particle in three dimensions we track the mean squared displacement as a function of time and use the relation [55]

$$D = \lim_{|t-t'|\to\infty} \frac{\langle(\mathbf{r}(t) - \mathbf{r}(t'))^2\rangle}{6(t-t')}. \tag{5.14}$$

Rather than using an infinite time displacement, what we actually do is look at the slope of $\langle(\mathbf{r}(t) - \mathbf{r}(t'))^2\rangle$ versus $6(t-t')$, which eventually becomes constant (equal to D). In keeping with our desire to simulate water, we decrease Δx to 2 nm and Δt to 0.001 ns in order to get significant thermal motion for the particle (this results in viscosity of water with $\tau/\Delta t = 0.75$ and sufficient numerical stability to allow large values of γ). The coupling parameter γ is recalibrated whenever we change to a

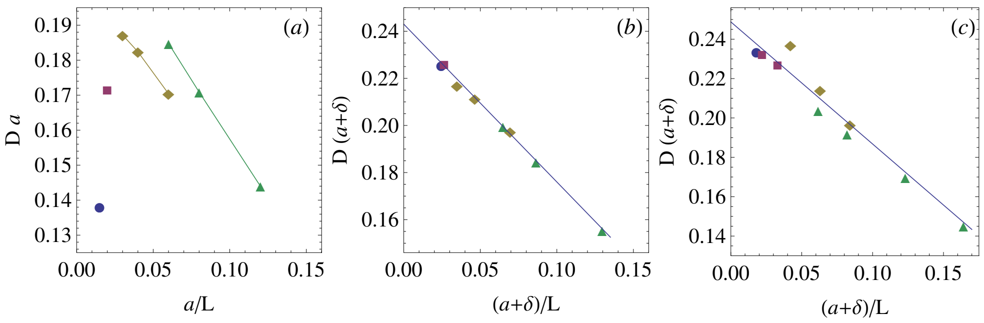

FIG. 5.8. *Diffusion coefficient D as a function mesh radius a, system size L, and a fitted "diffusion" radius $a + \delta$.* (a) *and* (b) *are for the Peskin stencil, and* (c) *is for the trilinear stencil. Different symbols are from runs with composite particles of different radii.* (b) *yields the value* 3.04 *and* (c) 2.82 *for the numerical constant A in* (5.15).

fullerene of different radius a. Other parameters in this section are $\rho = 998.2\,\mathrm{kg\,m^{-3}}$, $\eta = 1.0\,\mathrm{g\,m^{-1}\,s^{-1}}$, and $T = 330\,\mathrm{K}$.

The one remaining subtlety is that there are significant finite-size effects in the measurement of the diffusion coefficient [56, 57]. That is, we expect

$$D(L) = \frac{k_B T}{6\pi\eta a_{h,D}} - \frac{k_B T}{6\pi\eta}\frac{A}{L}, \tag{5.15}$$

where A is a dimensionless numerical constant with the theoretical prediction of 2.837 in the zero Reynolds number limit calculated in [56] from the Oseen tensor, and $a_{h,D}$ is a hydrodynamic radius that we expect to be equal to a_h determined from drag force and torque measurements. Thus, a plot of $D\,a_{h,D}$ versus $a_{h,D}/L$ should give a straight line onto which data from different radii should fall. If we assume $a_{h,D}$ is equal to the radius from the center to the location of the interpolating points of our composite particles (mesh radius), then such a plot is shown in Figure 5.8(a). Points from different radii clearly do not fall on the same line, suggesting that the diffusion radius is not the same as the mesh radius. If we fit to (5.15) with $a_{h,D} = a + \delta$, where a is the distance at which the surface nodes sit from the center of the composite particle, we get a good collapse of the data with $\delta = 0.38\,\Delta x$ for the Peskin stencil and $\delta = 0.12\,\Delta x$ for the trilinear stencil. This $a_{h,D}$ is within 1% of the values of $a_{h,F}$ and $a_{h,T}$ determined by drag force and torque measurements. In addition, the theoretical approximation of 2.837 is in excellent agreement with the fit parameter $A = 2.9 \pm 0.1$ of (5.15). Thus, choosing γ to give a consistent hydrodynamic radius results in nearly perfect agreement with the fluctuation-dissipation theorem (FDT) with no need for additional Langevin noise in (5.9) or (5.12).

We emphasize that the FDT will not generally be obeyed if γ is not chosen to give a consistent hydrodynamic radius. It is clear from (5.12) that if $\gamma = 0$, then the particle is not going to move, as the effective temperature felt by the particle is $T_m = 0$ for $\gamma = 0$. This was noted by Ahlrichs and Dünweg [24, 25]. With noise (as per [53, 54]) present in the LB fluid only, they measured the temperature T_m from the equipartition relation $(3/2)k_{\mathrm{B}}T_m = (1/2)m\langle \mathbf{v}^2\rangle$ (m is the mass of their point particle) by calculating the mean-squared velocity of a point particle. They observed that it depends strongly on γ [24, 25]. As they wished to work at arbitrary values of γ, they rectified this problem by adding Langevin noise to (5.12) and then subtracting an equal and opposite amount from the fluid to conserve momentum. The imposed fluctuation-dissipation relation had an amplitude that related the drag force to the bare (algorithmic) coupling γ rather than to the measured drag. By imposing the fluctuation-dissipation theorem in this way, they were naturally able to measure the temperature to be the input temperature T for any value of γ. The adjustment of the effective drag was made systematic in [24, 25], where the algorithmic parameter γ was increased until agreement with diffusion measurements from MD was attained. The developments of schemes with external added and subtracted Langevin noise are summarized in [58].

Instead, we have *no* added external Langevin noise in (5.12), as it leads to the result that $\langle(\mathbf{v}-\hat{\mathbf{u}})^2\rangle \sim T$, in contradiction to the no-slip/no-flow boundary condition we want on the surface. Our interpretation of the solid particle in the model is that the drag force imposes a constraint on the region of fluid overlapping the particle to move collectively, thus removing those degrees of freedom. We note that not only the measured temperature of the particle T_m depends strongly on γ, but so does the drag force. In fact, we find that T_m and the measured drag force have an identical dependence on γ in the absence of external Langevin noise (not surprising considering (5.12)). That is, the measured diffusion coefficient given by the Einstein relation as $D = k_{\mathrm{B}}T_m/C_d$, where C_d is the measured drag coefficient in absence of noise, is independent of γ. However, in this case, the particle will be at the same temperature as the fluid only if the hydrodynamic radius implied by (5.13) is consistent with a direct deterministic measurement of the drag force, such as those described in Figure 4.1. As this is the point at which we have already decided we need to operate, additional Langevin noise in the particle-fluid coupling equation, (5.9), is not necessary [49].

That the diffusion coefficient should be independent of γ can also be argued directly from an analysis of (5.12). The two-time correlation function $\langle\hat{u}_\alpha(t_1)\hat{u}_\beta(t_2)\rangle$ is not quite as obvious as the equal-time case (which is constrained to obey equipartition), especially in the vicinity of the particle, but fairly generally we may write it as

$$\langle\hat{u}_\alpha(t_1)\hat{u}_\beta(t_2)\rangle = \frac{k_BT}{\rho C_v}\delta_{\alpha\beta}R(t_2-t_1), \tag{5.16}$$

where the fluid response function $R(t)$ is a function of the fluid properties and the shape of the particle only [49]. The Green–Kubo relation [59] tells us that the diffusion coefficient D for the particle may be computed using the formal solution to (5.12) and the correlation function for $\hat{\mathbf{u}}$, (5.16), as

$$\begin{aligned} D &\equiv \frac{1}{3}\int_0^\infty \mathrm{d}t\langle\mathbf{v}(t)\cdot\mathbf{v}(0)\rangle \\ &= \frac{\gamma^2}{3m^2}\int_0^\infty \mathrm{d}t\int_{-\infty}^t \mathrm{d}t_1\int_{-\infty}^0 \mathrm{d}t_2\langle\hat{\mathbf{u}}(t_1)\cdot\hat{\mathbf{u}}(t_2)\rangle e^{\gamma(t-t_1-t_2)/m} \\ &= \frac{k_BT}{\rho C_v}\frac{\gamma^2}{m^2}\int_0^\infty \mathrm{d}t\int_{-\infty}^t \mathrm{d}t_1\int_{-\infty}^0 \mathrm{d}t_2 R(t_2-t_1)e^{\gamma(t-t_1-t_2)/m}. \end{aligned} \tag{5.17}$$

To proceed further, an explicit form of the response function is needed. The response function is dimensionless (from our definition in (5.16)). There can be long-time tails present due to hydrodynamics, but any finite system size will result in a finite correlation time. Under these assumptions, the explicit form is not that critical for calculating the general trends. For example, using $R(t) = \exp(-\Gamma|t|)$, where Γ is an

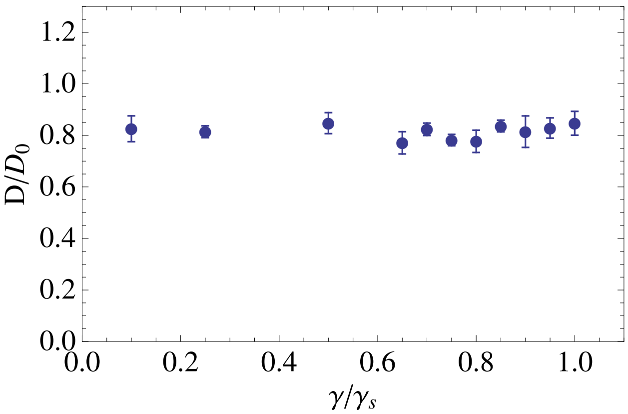

FIG. 5.9. *Diffusion coefficient* D *normalized by the expected result* $D_0 = k_B T/(6\pi\eta a_h)$ *for an infinite system versus the algorithmic coupling constant* γ *normalized by the value* γ_s *that yields a drag force in agreement with Stokes's formula for a particle of hydrodynamic radius* a_h*.*

inverse time constant related to the fluid response, gives the following result:

$$D = \frac{k_B T}{\rho C_v \Gamma}. \tag{5.18}$$

The main result here is that D does not explicitly depend on the algorithmic parameter γ if $R(t)$ has a finite correlation time. Hauge and Martin-Löf [49] have shown that both the slip and no-slip boundary conditions produce exactly the same long-time hydrodynamic tail in the velocity-autocorrelation function (VACF) of the particle, for which reason *the tail is no proof of correct hydrodynamic coupling* for a given boundary condition. In fact, we observe the tail to be independent of γ in our model. However, for the calibrated value of γ corresponding to no-slip, the VACF for our model is correct and the amount of fluid dragged with the particle agrees with theory [23].

Last, we tested in simulation how the diffusion coefficient depends on γ, when there is no external Langevin noise on the particle. We set up a small periodic box of size $(21\,\Delta x)^3$ and placed a 60-node composite particle of radius $a = 0.6\,\Delta x$ at its center. Again, we tracked the slope of the particle's mean square displacement versus time, from which we determined its diffusion coefficient for values of γ/γ_s ranging from 0.1 to 1.0, where γ_s is the value required to give a hydrodynamic radius based on the drag force of (5.5) equivalent to the particle node radius a. The results of these measurements are plotted in Figure 5.9. It is clear from the figure that D is independent of γ, thus confirming our theoretic assertion above (see (5.16)–(5.18)). However, D is also lower than that expected from the macroscopic fluctuation-dissipation relation of (5.13). Finite-size effects that we already quantified are the main source of this discrepancy, but the stencil also plays a part through δ. Note that in [24, 25] Ahlrichs and Dünweg showed the temperature measured from $(3/2)k_{\mathrm{B}}T_m = (1/2)m\langle \mathbf{v}^2\rangle$ to be different from that present in the LB fluid. We observe the same when $\gamma \neq \gamma_s$. However, just as the drag force and torque approach the no-slip result for $\gamma = \gamma_s$, we observe the temperature measured via equipartition to give the correct value at $\gamma = \gamma_s$.

6. Conclusions.

A simple Stokesian type of frictional coupling between solute particles and the velocity field of the solvent is a natural way to proceed in coarse-grained fluid modeling, and in the LB method in particular. Such frictional particle-fluid coupling has undergone significant developments in the last 10 years. First, in [24, 25], Ahlrichs and Dünweg measured the temperature experienced by a point particle and noticed that it depends on γ. To fix this, they added external Langevin noise directly to the particle's equation of motion to match with the target temperature T and adjusted γ to obtain a desired value for the diffusion coefficient. Then they inferred the hydrodynamic radius based on Stokes drag. Second, Chatterji and Horbach [39, 40] measured drag for a periodic array of particles in steady state with a balance between drag and gravitational force. They inferred the hydrodynamic radius from effective drag after finite-size scaling.

We have shown in the present paper that these two approaches do not necessarily give consistent hydrodynamic radii based on the drag force and viscous torque. To remedy this problem, we have shown that with a proper combination of stencils and composite particles, the coupling parameter γ can be chosen in a physically sensible and consistent way to match torque and drag in the no-slip limit. We have also demonstrated that our choice also gives the correct diffusion coefficient, i.e., the macroscopic fluctuation-dissipation theorem is obeyed, without externally added Langevin noise or an adjustable parameter of any kind. We also compared and contrasted in detail the use of different stencils (trilinear and Peskin) and different resolutions for small particles.

We conclude that our method provides a consistent hydrodynamic radius independent of means of measurement. We have shown that our algorithm produces congruous hydrodynamic radii whether moving walls induce the flow and the drag, the particle itself is moving, the particle experiences a torque, or we use diffusion as the basis of measurement. We have shown that in agreement with the general theoretic framework [49], no external Langevin noise is needed in the equations of motion for our consistent choice of γ in the no-slip limit. We also explained a misconception about using diffusion as a test for proper coupling to hydrodynamics by showing that the diffusion coefficient of a Brownian particle is independent of the algorithmic coupling parameter when the particle is driven by fluid fluctuations alone.

Finally, regarding hydrodynamic interparticle interactions we introduced a four-sphere arrangement to guarantee zero net velocity and torque in the system whereby we showed our scheme to agree fully with Oseen and RP theories in the relevant limit of small Reynolds number and intermediate distances. As particles approach each other, Oseen theory breaks down expectedly while the RP tensor remains valid for smaller particle separations. We explored the full range of hydrodynamic forces and characterized the effect of finite propagation speed of hydrodynamic interactions, which results in a lag that can drastically change the hydrodynamic force on a particle. This observation makes some studies on colloidal dynamics based on the discretization of the Oseen or RP tensors suspect unless the particle speed is sufficiently small. This effect should be particularly significant in shear flows.

Appendix. Forcing terms.

We take the BGK approximation of the continuum Boltzmann equation [32],

$$\begin{aligned} &\left(\frac{\partial}{\partial t} + \frac{\partial x_\gamma}{\partial t}\frac{\partial}{\partial x_\gamma} + \frac{\partial p_\gamma}{\partial t}\frac{\partial}{\partial p_\gamma}\right) f = -\frac{1}{\tau}(f - f^{\mathrm{eq}}) \\ &\Leftrightarrow (\partial_t + v_\gamma \partial_\gamma) f = -\frac{1}{\tau}(f - f^{\mathrm{eq}}) - F_\gamma \partial_{p_\gamma} f, \end{aligned} \tag{A.1}$$

as our starting point. The forcing term on the right-hand side is approximated to lowest order as $F_\gamma \partial_{p_\gamma} f \approx F_\gamma \partial_{p_\gamma} f^{\mathrm{eq}}$. Our lattice equilibria f_i^{eq} are the well-known second-order expansions in Hermite polynomials,

$$f_i^{\mathrm{eq}} = w_i \left(\rho + \frac{3}{v_c^2} p_\lambda e_{i\lambda} + \frac{9H_{\lambda\nu}}{2v_c^4} \left(P_{\lambda\nu} + \frac{p_\lambda p_\nu}{\rho} - \frac{\rho v_c^2}{3} \delta_{\lambda\nu} \right) \right), \tag{A.2}$$

where $H_{\lambda\nu} = e_{i\lambda} e_{i\nu} - (v_c^2/3)\delta_{\lambda\nu}$ and w_i are the weights for the particular DdQn lattice. We have written the equilibria in terms of the momentum densities p_λ to evaluate the derivative in the forcing term of the BGK equation as

$$\partial_{p_\gamma} f_i^{\mathrm{eq}} = w_i \left(-\frac{3}{\rho v_c^2} p_\gamma + \frac{3}{v_c^2} e_{i\gamma} + \frac{9}{\rho v_c^4} p_\lambda e_{i\gamma} e_{i\lambda} \right). \tag{A.3}$$

The zeroth, first, and second moments of the forcing terms are then obtained by direct calculation to be

$$\begin{aligned} &\sum_i F_\gamma \partial_{p_\gamma} f_i^{\mathrm{eq}} \\ &= F_\gamma \frac{3}{v_c^2} \left(-\frac{p_\gamma}{\rho} \sum_i w_i + \sum_i w_i e_{i\gamma} + \frac{3p_\lambda}{\rho v_c^2} \sum_i w_i e_{i\gamma} e_{i\lambda} \right) \\ &= F_\gamma \frac{3}{v_c^2} \left(-\frac{p_\gamma}{\rho} \cdot 1 + 0 + \frac{3p_\lambda}{\rho v_c^2} \cdot \frac{v_c^2}{3} \delta_{\gamma\lambda} \right) = 0. \end{aligned} \tag{A.4}$$

Similarly, the first and second moments are

$$\begin{aligned} &\sum_i F_\gamma (\partial_{p_\gamma} f_i^{\mathrm{eq}}) e_{i\alpha} = F_\alpha; \\ &\sum_i F_\gamma (\partial_{p_\gamma} f_i^{\mathrm{eq}}) e_{i\alpha} e_{i\beta} = u_\alpha F_\beta + F_\alpha u_\beta, \end{aligned} \tag{A.5}$$

where we have made use of relations $\sum_i w_i e_{i\alpha} e_{i\beta} e_{i\gamma} = 0$ and $\sum_i w_i e_{i\alpha} e_{i\beta} e_{i\gamma} e_{i\lambda} = (v_c^4/9)(\delta_{\alpha\beta}\delta_{\gamma\lambda} + \delta_{\alpha\gamma}\delta_{\beta\lambda} + \delta_{\alpha\lambda}\delta_{\beta\gamma})$. The moments agree with those from lengthy multiscale expansions and the discretized derivation in [60].

REFERENCES

[1] T. G. M. V. de Ven, *Colloidal Hydrodynamics*, Academic Press, New York, 1989.

[2] W. Sparreboom, A. van der Berg, and J. C. T. Eijkel, *Transport in nanofluidic systems: A review of theory and applications*, New J. Phys., 12 (2010), 015004.

[3] G. Stokes, *Mathematical and Physical Papers Volume* I, Cambridge University Press, Cambridge, UK, 1880; also available online from http://www.archive.org/details/mathphyspapers01stokrich.

[4] J. Happel and H. Brenner, *Low Reynolds Number Hydrodynamics*, Kluwer, Boston, 1983.

[5] G. K. Batchelor, *An Introduction to Fluid Mechanics*, Cambridge University Press, Cambridge, UK, 1967.

[6] D. J. Jeffrey and Y. Onishi, *Calculation of the resistance and mobility functions for two unequal rigid spheres in low-Reynolds-number flow*, J. Fluid Mech., 139 (1984), pp. 261–290.

[7] D. J. Jeffrey, *The calculation of the low Reynolds number resistance functions for two unequal spheres*, Phys. Fluids A, 4 (1992), pp. 16–29.

[8] C. W. Oseen, *Hydrodynamik*, Akademische Verlag, Leipzig, 1927.

[9] J. Rotne and S. Prager, *Variational treatment of hydrodynamic interaction in polymers*, J. Chem. Phys., 50 (1969), pp. 4831–4837.

[10] J. M. Yeomans, *Phase ordering in fluids*, in Annual Reviews of Computational Physics VII, D. Stauffer, ed., World Scientific Publishing, Singapore, 1999, pp. 61–84.

[11] M. R. Swift, W. R. Osborn, and J. M. Yeomans, *Lattice Boltzmann simulation of nonideal fluids*, Phys. Rev. Lett., 75 (1995), pp. 830–833.

[12] I. Pagonabarraga, *Lattice Boltzmann modeling of complex fluids: Colloidal suspensions and fluid mixtures*, in Novel Methods in Soft Matter Simulations, Lecture Notes in Phys. 640, Springer-Verlag, Berlin, Heidelberg, 2004, pp. 279–309.

[13] K. Mattila, J. Hyväluoma, J. Timonen, and T. Rossi, *Comparison of implementations of the lattice-Boltzmann method*, Comput. Math. Appl., 55 (2008), pp. 1514–1524.

[14] M. E. Cates, K. Stratford, R. Adhikari, P. Stansell, J.-C. Desplat, I. Pagonabarraga, and A. J. Wagner, *Simulating colloid hydrodynamics with lattice Boltzmann method*, J. Phys. Condens. Matter, 16 (2004), pp. S3903–S3915.

[15] V. Lobaskin and B. Dünweg, *A new model for simulating colloidal hydrodynamics*, New J. Phys., 6 (2004), 54.

[16] V. Lobaskin, B. Dünweg, and C. Holm, *Electrophoretic mobility of a charged colloidal particle: A computer simulation study*, J. Phys. Condens. Matter, 16 (2004), pp. S4063–S4073.

[17] A. M. Roma, C. S. Peskin, and M. J. Berger, *An adaptive version of the immersed boundary method*, J. Comput. Phys., 153 (1999), pp. 509–534.

[18] M.-C. Lai and C. S. Peskin, *An immersed boundary method with formal second-order accuracy and reduced numerical viscosity*, J. Comput. Phys., 160 (2000), pp. 705–719.

[19] C. S. Peskin, *The immersed boundary method*, Acta Numer., 11 (2002), pp. 479–517.

[20] T. T. Bringley and C. S. Peskin, *Validation of a simple method for representing spheres and slender bodies in an immersed boundary method for Stokes flow on an unbounded domain*, J. Comput. Phys., 227 (2008), pp. 5397–5425.

[21] R. W. Nash, R. Adhikari, and M. E. Cates, *Singular forces and pointlike colloids in lattice Boltzmann hydrodynamics*, Phys. Rev. E (3), 77 (2008), 026709.

[22] R. Adhikari, K. Stratford, M. E. Cates, and A. J. Wagner, *Fluctuating lattice Boltzmann*, Europhys. Lett., 71 (2005), pp. 473–479.

[23] S. T. T. Ollila, C. Denniston, M. Karttunen, and T. Ala-Nissila, *Fluctuating lattice-Boltzmann model for complex fluids*, J. Chem. Phys., 134 (2011), 064902.

[24] P. Ahlrichs and B. Dünweg, *Lattice-Boltzmann simulation of polymer-solvent systems*, Internat. J. Modern Phys. C, 9 (1998), pp. 1429–1438.

[25] P. Ahlrichs and B. Dünweg, *Simulation of a single polymer chain in solution by combining lattice Boltzmann and molecular dynamics*, J. Chem. Phys., 111 (1999), pp. 8225–8239.

[26] A. Einstein, *Über die von der molekularkinetischen Theorie der Wärme geforderte Bewegung von in ruhenden Flüssigkeiten suspendierten Teilchen*, Ann. Phys., 322 (1905), pp. 549–560.

[27] L. D. Landau and E. M. Lifschitz, *Fluid Mechanics*, 2nd ed., Pergamon Press, Oxford, UK, 1987.

[28] G. S. Kell, *Isothermal compressibility of liquid water at 1 atm*, J. Chem. Eng. Data, 15 (1970), pp. 119–122.

[29] S. Chen and G. D. Doolen, *Lattice Boltzmann method for fluid flows*, in Annual Review of Fluid Mechanics, Annu. Rev. Fluid Mech. 30, Annual Reviews, Palo Alto, CA, 1998, pp. 329–364.

[30] S. Succi, *The Lattice Boltzmann Equation for Fluid Dynamics and Beyond*, Oxford University Press, New York, 2001.

[31] M. C. Sukop and D. T. J. Thorne, *Lattice Boltzmann Modeling: An Introduction for Geoscientists and Engineers*, Springer, Berlin, 2005.

[32] P. L. Bhatnagar, E. P. Gross, and M. Krook, *A model for collision processes in gases.* I. *Small amplitude processes in charged and neutral one-component systems*, Phys. Rev., 94 (1954), pp. 511–525.

[33] J. C. Strikwerda, *Finite Difference Schemes and Partial Differential Equations*, 2nd ed., SIAM, Philadelphia, 2004.

[34] F. Higuera, S. Succi, and R. Benzi, *Lattice gas dynamics with enhanced collisions*, Europhys. Lett., 9 (1989), pp. 345–349.

[35] F. J. Higuera and J. Jiménez, *Boltzmann approach to lattice gas simulations*, Europhys. Lett., 9 (1989), pp. 663–668.

[36] R. L. Burden and J. D. Faires, *Numerical Analysis*, 8th ed., Thomson, Belmont, CA, 2005.

[37] C. J. Smith and C. Denniston, *Elastic response of a nematic liquid crystal to an immersed nanowire*, J. Appl. Phys., 101 (2007), 014305.

[38] CCL.net, http://server.ccl.net/cca/data/fullerenes/index.shtml (1999).

[39] A. Chatterji and J. Horbach, *Combining molecular dynamics with Lattice Boltzmann: A*

hybrid method for the simulation of (charged) colloidal systems, J. Chem. Phys., 122 (2005), 184903.

[40] A. Chatterji and J. Horbach, *Electrophoretic properties of highly charged colloids: A hybrid molecular dynamics/lattice Boltzmann simulation study*, J. Chem. Phys., 126 (2007), 064907.

[41] N. Liron and S. Mochon, *Stokes flow for a stokeslet between two parallel flat plates*, J. Eng. Math., 10 (1976), pp. 287–303.

[42] A. Goldman, R. Cox, and H. Brenner, *Slow viscous motion of a sphere parallel to a plane wall*—II *Couette flow*, Chem. Eng. Sci., 22 (1967), pp. 653–660.

[43] A. Goldman, R. Cox, and H. Brenner, *Slow viscous motion of a sphere parallel to a plane wall*—I *Motion through a quiescent fluid*, Chem. Eng. Sci., 22 (1967), pp. 637–651.

[44] L. Durlofsky, J. F. Brady, and G. Bossis, *Dynamic simulation of hydrodynamically interacting particles*, J. Fluid Mech., 180 (1986), pp. 21–49.

[45] J. W. Swan and J. F. Brady, *Simulation of hydrodynamically interacting particles near a no-slip boundary*, Phys. Fluids, 19 (2007), 113306.

[46] C. W. J. Beenakker, *Ewald sum of the Rotne–Prager tensor*, J. Chem. Phys., 85 (1986), pp. 1581–1582.

[47] O. B. Usta, A. J. C. Ladd, and J. E. Butler, *Lattice-Boltzmann simulations of the dynamics of polymer solutions in periodic and confined geometries*, J. Chem. Phys., 122 (2005), 094902.

[48] D. Mukherji, G. Bartels, and M. Müser, *Scaling laws of single polymer dynamics near attractive surfaces*, Phys. Rev. Lett., 100 (2008), 068301.

[49] E. H. Hauge and A. Martin-Löf, *Fluctuating hydrodynamics and Brownian motion*, J. Statist. Phys., 7 (1973), pp. 259–281.

[50] R. Zwanzig and M. Bixon, *Compressibility effects in the hydrodynamic theory of Brownian motion*, J. Fluid Mech., 69 (1975), pp. 21–25.

[51] Y. Iwashita, Y. Nakayama, and R. Yamamoto, *A numerical model for Brownian particles fluctuating in incompressible fluids*, J. Phys. Soc. Japan, 77 (2008), 074007.

[52] T. T. Pham, U. D. Schiller, J. R. Prakash, and B. Dünweg, *Implicit and explicit solvent models for the simulation of a single polymer chain in solution: Lattice Boltzmann versus Brownian dynamics*, J. Chem. Phys., 131 (2009), 164114.

[53] A. J. C. Ladd, *Numerical simulations of particulate suspensions via a discretized Boltzmann equation. Part* 1. *Theoretical foundation*, J. Fluid Mech., 271 (1994), pp. 285–309.

[54] A. J. C. Ladd, *Numerical simulations of particulate suspensions via a discretized Boltzmann equation. Part* 2. *Numerical results*, J. Fluid Mech., 271 (1994), pp. 311–339.

[55] D. Frenkel and B. Smit, *Understanding Molecular Simulation*, Academic Press, London, 2002.

[56] H. Hasimoto, *On the periodic fundamental solutions of the Stokes equations and their application to viscous flow past a cubic array of spheres*, J. Fluid Mech., 5 (1959), pp. 317–328.

[57] A. Malevanets and J. M. Yeomans, *Dynamics of short polymer chains in solution*, Europhys. Lett., 52 (2000), pp. 231–237.

[58] B. Dünweg and A. J. C. Ladd, *Lattice Boltzmann simulations of soft matter systems*, in Advanced Computer Simulation Approaches for Soft Matter Sciences III, Adv. Polym. Sci. 221, Springer, Berlin, 2009, pp. 89–166.

[59] R. Kubo, M. Toda, and N. Hashitsume, *Statistical Physics* II, 2nd ed., Springer, Berlin, 1995.

[60] N. S. Martys, X. Shan, and H. Chen, *Evaluation of the external force term in the discrete Boltzmann equation*, Phys. Rev. E (3), 58 (1998), pp. 6855–6857.